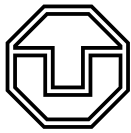




Non Reciprocal Behavior of Spin Waves in Coupled Layers

Peter Matthies

Master Thesis



Non Reciprocal Behavior of Spin Waves in Coupled Layers

Peter Matthies

Born on: 07.08.1994 in Dresden

Course: Master of Physics

Discipline: Electronic Properties of Solids

Matriculation number: 4517380

Matriculation year: 2015

Master Thesis

to achieve the academic degree

Master of Science (M.Sc.)

First referee

Prof. Dr. rer. nat. Jürgen Faßbender

Second referee

Prof. Dr. rer. nat. Olav Hellwig

Supervisor

Dr. rer. nat. Helmut Schultheiß

Submitted on: 30.10.2017



Task for the preparation of a Master Thesis

Course: Master of Physics
Discipline: Electronic Properties of Solids
Name: **Peter Matthies**
Matriculation number: 4517380
Matriculation year: 2015
Title: **Non Reciprocal Behavior of Spin Waves in Coupled Layers**

Objectives of work

1. Learning of sample production via Electron Beam Lithography
2. Learning of the principles of Brillouin Light Scattering and the physics behind it
3. Investigation of the spin-wave behavior in coupled layers

Focus of work

- Conventional Brillouin Light Scattering Setup (BLS)
- Investigation of non-reciprocal dispersion relation of spin waves in coupled layers
- Electron Beam Lithography for sample production and antenna patterning
- Investigation of spin-wave propagation via Brillouin Light Scattering Microscope (μ BLS) in coupled layers
- Investigation of caustic emission via Brillouin Light Scattering Microscope (μ BLS) in coupled layers

First referee: Prof. Dr. rer. nat. Jürgen Faßbender
Second referee: Prof. Dr. rer. nat. Olav Hellwig
Supervisor: Dr. rer. nat. Helmut Schultheiß
Issued on: 30.04.2017
Due date for submission: 30.10.2017

Prof. Dr. rer. nat. Jürgen Faßbender
Supervising professor

I dedicate this to my beloved parents.

Abstract

This thesis investigates the possible non-reciprocal spin-wave dispersion in coupled bilayer magnetic films. Non-reciprocal spin-wave propagation offers promising opportunities for information technologies of the future. The samples consisted of two coupled magnetic layers separated by a non-magnetic spacing layer. The coupling of the two layers allows for experimental control of the current state of the bilayer system. Depending on the relative alignment of the magnetization vectors between the two layers non-reciprocal spin-wave propagation has been predicted theoretically.

The samples were investigated by means of Brillouin Light Scattering. During the work on this thesis, a conventional Brillouin Light Scattering setup was assembled. This setup was used for measurements of thermally excited spin waves. Additionally, the spin-wave propagation in patterned microstructures was explored with a Brillouin Light Scattering microscope. The spin-wave dynamics was excited by local magnetic fields induced by patterned gold antenna structures. Possibilities of caustic beams radiation were explored with special point-source like antennas.

The main goals of the work where the experimental observation of the non-reciprocal spin-wave dispersion and the caustic beam radiation in the bilayer systems. The angle of caustic beam radiation with respect to the current state of the bilayer system and the excitation frequency was explored as well.

Contents

Abstract	ix
1 Introduction	1
2 Theory	3
2.1 Landau-Lifshitz-Gilbert equation	3
2.2 The Effective Magnetic Field	4
2.2.1 Demagnetizing field	4
2.2.2 Exchange field	5
2.3 Spin waves	6
2.3.1 Infinite solid	7
2.3.2 Dispersion of a thin film	8
2.4 Spin waves in coupled bilayers	9
2.4.1 Zeeman Field	10
2.4.2 Uniaxial anisotropy	10
2.4.3 Exchange field	11
2.4.4 Dipolar fields	11
2.4.5 Interlayer Exchange Interaction	12
2.5 Theoretical Predictions	12
3 Experimental Setup	17
3.1 Brillouin-Light-Scattering (BLS)	17
3.1.1 Fabry-Pérot Interferometer	19
3.1.2 Tandem-Fabry-Pérot-Interferometer	21
3.2 Conventional Brillouin Light Scattering	23
3.3 Micro-focused Brillouin Light Scattering (μ BLS)	24
4 Results and Discussion	29
4.1 Samples overview	29
4.2 BLS measurements	29
4.3 Micro-BLS measurements	35
4.3.1 Sample preparation	35
4.3.2 Eigenmode spectra	36
4.3.3 Caustics measurements	43
5 Summary and Outlook	49
Statement of authorship	57

1 Introduction

The noblest pleasure is the joy of understanding

(Leonardo da Vinci)

Recent advances in spin dynamics gave a perspective on information processing purely based on the quasiparticles of spin waves - magnons. This is currently a promising direction for the beyond-CMOS computing technology (CMOS: complementary metal-oxide-semiconductor). The wave-based computing is attractive, because wave phase could provide an additional degree of freedom in the data processing. For example, in [1] the realization of different types of logic gates, that use traveling spin waves in the GHz range, was shown. Other works [2, 3] include conceptual designs of possible logic circuitry, explore the advantages of data transfer without the usage of electrical currents and demonstrate the scaling possibilities as magnonic logic circuits allow for THz-frequency operation. Electrical demonstrations of spin-wave interference [4] describe the possibility of spin-wave logic operation and the control over the phase of spin waves via the configuration of the RF excitation antenna. Regarding spin-wave transport, significant amount of research is directed towards exploration of the possibilities of spin-wave propagation on the nanoscale [5], taking advantage of the intrinsic properties of magnetic materials such as domain walls.

Strong non-linearities coming from the anisotropic nature of spin waves generate interesting effects such as nondiffractive subwavelength spin-wave beams [6]. This opens ways to non-Boolean computing [7]. A corresponding example is a three-input combiner as a majority gate [8] with the possibility of substitution of several tens of CMOS transistors. Another example is a spin-wave multiplexer [9], which can be seen as a fundamental building block of the future magnon-based logic devices.

Discoveries of non reciprocal effects in materials with strong antisymmetric exchange interaction, known as the Dzyaloshinskii-Moriya interaction (DMI), only strengthened those ideas [10, 11]. Caustic beams interference in ultrathin ferromagnetic films with DMI [12] attracts more attention to the investigation of caustic beam radiation in general. Additionally, isotropic transmission of spin waves in exchange coupled multilayers [13] without external magnetic fields opens new possibilities in the design of spin-wave devices.

The thesis describes investigation of the non-reciprocal dispersion of spin waves in coupled bilayers. Coupled bilayers prove to be much more flexible in application as they can have both reciprocal as well as non-reciprocal spin-wave dispersion depending on the current magnetization alignment of the two layers. Mechanisms such as exchange bias or the interlayer exchange interaction allow for control of the current state of the bilayer system with external magnetic fields in real devices. Moreover, controlled spin-wave caustic beam emission is very attractive for the spin-wave devices of the future.

2 Theory

This chapter describes the fundamental theoretical concepts important for the understanding of the experiments done in connection with this Master thesis. First, the Landau-Lifshitz-Gilbert equation for the magnetization dynamics is discussed. Second, the spin waves theory for a single layer is described, following the theoretical expressions given in [15]. Lastly, the approach for a two coupled bilayer system is shown.

2.1 Landau-Lifshitz-Gilbert equation

A well known and fundamental equation describing the spin dynamics is the Landau-Lifshitz equation [14]. It is an equation of motion for the magnetization in an effective magnetic field. In combination with the Maxwell-Equations, one can derive all the equations of magnetization dynamics important for this thesis. Although the magnetic properties of a solid have a quantum-mechanical origin the Landau-Lifshitz equation can be derived semi-classically.

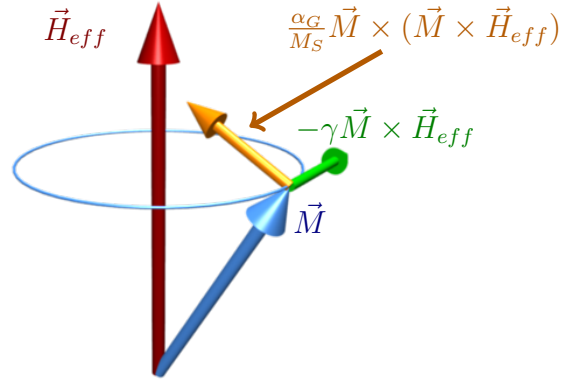


Figure 2.1: A schematical illustration to the Landau-Lifshitz-Gilbert equation. The magnetization M starts precessing around the effective magnetic field H_{eff} because of the acting torque. The Gilbert damping term (orange) brings the magnetization to the equilibrium position along the effective field direction. Image is taken from [15]

If an atomic magnetic moment μ_m is misaligned with respect to the effective magnetic field H_{eff} a torque of the following form will be acting on it:

$$D = \mu_m \times H_{eff} \quad (2.1)$$

As the torque is the time derivative of the angular momentum the equation (2.1) can be rewritten taking into account the connection between the magnetic moment and the angular momentum via the gyromagnetic ratio $L = -\gamma \cdot \mu_m$:

$$D = \frac{dL}{dt} = -\gamma \frac{d\mu_m}{dt} = \mu_m \times H_{eff}, \quad (2.2)$$

where the gyromagnetic ratio is given by $\gamma = \frac{g\mu_B}{\hbar}$, g represents the Landé factor of the electron, $\mu_B = \frac{e\hbar}{2m_e}$ is the Bohr's Magnetron and the \hbar is the reduced Plank's constant.

Summing up all the magnetic moments leads to the equation for the magnetization:

$$\frac{dM}{dt} = -\gamma M \times H_{eff}. \quad (2.3)$$

This is the original form of the Landau-Lifshitz equation derived by them in 1935 for the first time [14]. According to this form of the equation, the magnetization would precess without any losses once it is out of the equilibrium direction. In reality, however, damping effects will drive the magnetization back into its equilibrium direction along the effective magnetic field. To account for the damping T.L. Gilbert introduced a third phenomenological term to the equation (2.3). This resulted in the well known *Landau-Lifshitz-Gilbert equation* [16]:

$$\frac{dM}{dt} = -\gamma M \times H_{eff} + \frac{\alpha_G}{M_s} M \times (M \times H_{eff}), \quad (2.4)$$

where α - dimensionless Gilbert-Damping parameter, M_s - saturation magnetization. The according quantum-mechanical derivations can be found in [17, 18].

2.2 The Effective Magnetic Field

The effective magnetic field in the Eq. (2.21) consists of many components.

$$H_{eff} = H_0 + H(t) + H_{ani} + H_{demag} + H_{Ex} + H_{iEx} \quad (2.5)$$

Here H_0 and $H(t)$ describe the static and the time-varying components of the external magnetic fields. H_{ani} stands for the anisotropic field coming from the crystallographic structure of the solid. The magnetic surface charges create demagnetizing fields H_{demag} via the dipole-dipole interaction and the H_{Ex} term comes from the exchange interaction. Finally, the last term is given by the interlayer exchange interaction, which is important in multi-layer systems. Next sections will address the contributions of the demagnetizing field and the exchange field in more detail.

2.2.1 Demagnetizing field

Inside a long homogeneous solid the magnetic moments generate dipolar fields. These fields cancel out for neighboring magnetic moments in volume however not for the surface. The magnetic moments on the surface generate an effective magnetic field via the dipolar interaction. This field is called as the *demagnetizing field* or the *stray field*.

The dipolar magnetic field generated by a single moment μ_m on the distance of r is given by:

$$H_d = \frac{3r(r \cdot \mu_m)}{r^5} - \frac{\mu_m}{r^3} \quad (2.6)$$

The demagnetizing field should fulfill Maxwell's magnetostatic equations:

$$\nabla \times H_{demag} = 0 \quad (2.7)$$

$$\nabla \cdot B = \nabla \cdot (H_{demag} + 4\pi M) = 0 \quad (2.8)$$

The usage of the magnetostatic approximation is justified by the fact, that the phase velocity of the investigated in this work spin waves is smaller than the speed of light by at least 3 orders of magnitude.

As the rotation of a gradient field is always zero one can define the H_{demag} in the Eq. (2.7) as a gradient of a scalar potential ϕ_M :

$$H_{demag} = -\nabla\phi_M. \quad (2.9)$$

The second Maxwell equation can be then rewritten into a magnetostatic Poisson-equation:

$$\Delta\phi_M = -\rho_M, \quad (2.10)$$

where the divergence of the magnetization can be interpreted as the effective magnetic charge density:

$$\rho_M = -4\pi\nabla \cdot M. \quad (2.11)$$

Analogous to electrostatics the solution of a Poisson-equation without boundary conditions is given by the Poisson-Integral:

$$\phi_M(r) = \frac{1}{4\pi} \int \frac{\rho_M}{|r - r'|} dr' = - \int \frac{\nabla' \cdot M(r')}{|r - r'|} dr'. \quad (2.12)$$

In a solid however the magnetization is limited to a certain area, so the boundary conditions must be taken into account. The integral is then split into volume and surface integrals as follows:

$$\phi_M(r) = \phi_V(r) + \phi_S(r) = - \int_V \frac{\nabla' \cdot M(r')}{|r - r'|} dr' + \oint_{\partial V} \frac{n(r') \cdot M(r')}{|r - r'|} dF'. \quad (2.13)$$

The first integral gives contribution only when an inhomogeneous magnetization distribution over the volume V is present. Only then is the volume charge density $\lambda_M = -4\pi\nabla(r) \cdot M(r)$ non zero. Accordingly, the effective surface charge density is given by $\sigma_M = 4\pi n(r) \cdot M(r)$, where $n(r)$ is the normal vector with respect to the surface ∂V . Therefore, only when the magnetization is not parallel to the surface there is a non zero surface charge density. Without external magnetic fields because of energy minimization the magnetization in a limited volume will be distributed so that it is parallel to the surface and that internal divergence is equal zero ($\nabla \cdot M = 0$). Of course the distribution can be different after addition of other energy contributions such as the exchange energy, for example.

2.2.2 Exchange field

The exchange energy is based on the spin-spin interaction of the electrons in a solid and is thus a purely quantum mechanical effect. Since electrons are fermions, they must obey the Pauli principle and have an antisymmetric total wave function, which can be obtained as a product of the space-dependent and the spin-dependent wavefunctions respectively. Therefore, two states are possible, in which the spins of the electrons are either parallel or antiparallel. As a measure of the energy splitting between these two states, the exchange constant J^{ex} , also referred to as exchange integral, is defined. With J^{ex} a spin Hamiltonian can be set up in the so-called Heisenberg model:

$$\mathcal{H}_{ex} = -2 \sum_{i \neq j}^n J_{ij}^{ex} S_i \cdot S_j \quad (2.14)$$

Depending on the sign of the exchange integral, a parallel ($J^{ex} > 0$) or antiparallel ($J^{ex} < 0$) orientation of the individual spins S_i and S_j is preferred. Since the coupling constant J_{ij}^{ex}

strongly depends on the overlap integral of the one-particle wave functions of the atoms i and j , the exchange interaction is significantly shorter than the previously described dipole-dipole interaction. It is therefore sufficient to calculate the exchange energy for a single spin S_i only over the number Z of the nearest neighbors NN instead of summation over all spins:

$$E_i^{ex} = -2 \sum_j^{NN} J_{ij}^{ex} S_i \cdot S_j = -2 S_i \cdot \sum_j^{NN} J_{ij}^{ex} S_j = \frac{2\mu_i}{g\mu_B} \cdot \sum_j^{NN} J_{ij}^{ex} S_j. \quad (2.15)$$

The last step used the relation between the spin S and the magnetic moment $\mu = g\mu_B S$. Now the exchange energy can be viewed as Zeeman-energy $E_Z = -\mu_0 \mu_i H_{ex}$ of a magnetic moment μ_i in a so-called exchange field H_{ex} :

$$H_{ex} = -\frac{2}{g\mu_0\mu_B} \sum_j^{NN} J_{ij}^{ex} S_j \quad (2.16)$$

Under the assumption of constant exchange integral J_{ex} for all of the neighboring spins, the Eq. (2.16) can be quasi-classically simplified for the whole spin system:

$$E_{ex} = -2J_{ex}ZS^2 \sum_{i \neq j}^{NN} \cos(\varphi_{ij}), \quad (2.17)$$

where φ_{ij} is the angle between the two neighboring spins S_i and S_j . Additionally, assuming small angles φ_{ij} the cosine in Eq. (2.17) can be expanded into a series. The transition from single spins to macroscopic magnetization M ultimately yields an expression for the exchange energy density (constant terms neglected):

$$\varepsilon_{ex} = \frac{2A}{M_s^2} (\nabla \cdot M)^2 = \frac{2A}{M_s^2} M \cdot \Delta M. \quad (2.18)$$

The parameter A is defined as the exchange constant:

$$A = \frac{S^2 a^2 J_{ex} N}{2}, \quad (2.19)$$

where a is the lattice constant and N is the number of nearest neighbors per unit volume. Because of $H_{ex} = -\nabla \varepsilon_{ex}$, the exchange field can also be written as:

$$H_{ex} = \frac{2A}{M_s^2} \Delta M = \frac{\lambda_{ex}}{M_s} \Delta M, \quad (2.20)$$

where $\lambda_{ex} = \frac{2A}{M_s}$ is called as the exchange-stiffness constant.

2.3 Spin waves

Spin waves are the fundamental excitations of the magnetization. They represent the magnetic analogon of the vibrational excitations of a solid, the phonons. The wavelength of a spin-wave in an infinite solid is not defined by an amplitude modulation in contrast to phonons. All magnetic moments precess with the same frequency and amplitude with a variation in the phase of the precession motion, which defines the wavelength of the spin-wave (see Fig. 2.2). The energy of a spin-wave and, therefore, its frequency is essentially defined by two coupling mechanisms. If the wavelength is big the phase difference between two neighboring spins is small, which means that the relative tilting of two neighboring spins to each other is small. In such case, the exchange energy is negligible and the spin-wave frequency is therefore dominated by the long-range dipole-dipole interaction. For small wavelengths the phase difference is bigger and thus the tilting of two neighboring spins to each other is bigger. Here, the exchange interaction gives the main contribution to the energy of the spin-wave.

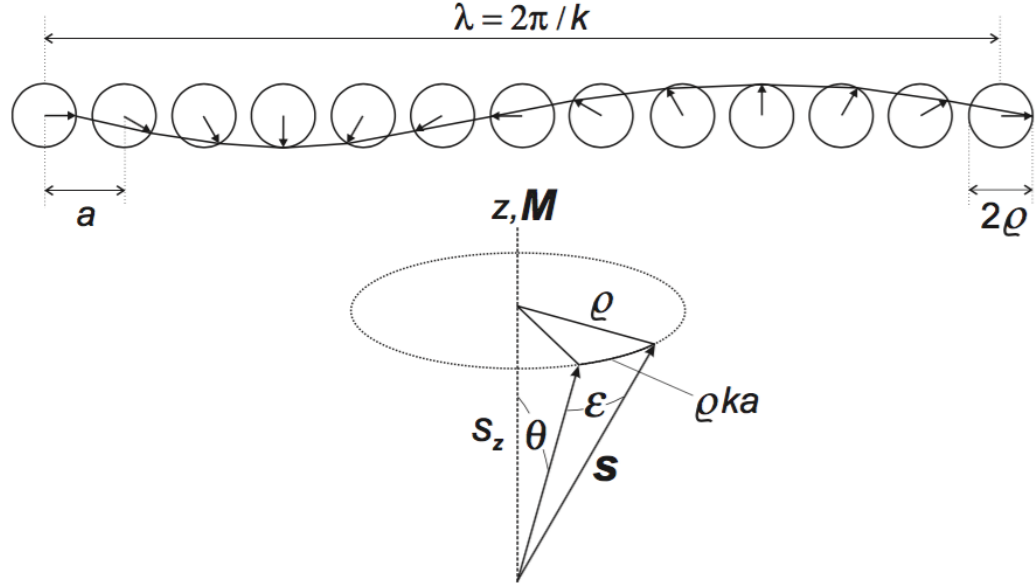


Figure 2.2: An example of a spin wave. The upper part of the picture describes the motion in the plane perpendicular to the magnetization. If λ is the wavelength, then $\lambda = Na$, where a is the lattice parameter and N is the number of involved sites. The lower part of the figure shows the angle ε between neighboring spins and its connection to the amplitude ρ . Image from [19]

2.3.1 Infinite solid

As already discussed above the temporal evolution magnetization of magnetization in a thin magnetic layer is described by the Landau-Lifshitz(LL) equation:

$$\frac{dM(r,t)}{dt} = -\gamma M(r,t) \times H^{eff}(r,t) \quad (2.21)$$

Here we will discard the damping for the sake of simplicity of analytical calculations. Most elementary case of all magnetic moments precessing uniformly in phase corresponds to a spin-wave of an infinite wavelength ($k=0$) and is known as the Ferromagnetic Resonance (FMR). As in this case all the spins are precessing at the same frequency and phase, they are parallel to each other in any given point of time. For this reason, the contribution of the exchange energy can be neglected.

To calculate the precession frequency one needs to solve the LL-equation (Eq. (2.21)) with addition of the magnetostatic Maxwell-equations. For an infinite solid magnetized in z -direction the magnetization as well as the magnetic field are split in respective static and dynamic components. Moreover, a harmonic time dependence of the dynamic components is assumed:

$$M = M_0 + m(t) = \begin{pmatrix} m_x e^{i\omega t} \\ m_y e^{i\omega t} \\ M_0 \end{pmatrix}, \quad (2.22)$$

$$H = H_0 + h(t) = \begin{pmatrix} h_x e^{i\omega t} \\ h_y e^{i\omega t} \\ H_0 \end{pmatrix}. \quad (2.23)$$

For small dynamic amplitudes $m_x, m_y \ll M_0$ and $h_x, h_y \ll H_0$ the LL-equation can be linearized in the precession frequency. The result is a so-called Kittel-Formula for an isotropic

solid [20]:

$$f = \frac{\gamma}{2\pi} \sqrt{(H_0 + 4\pi M_s) H_0}. \quad (2.24)$$

This formula describes the frequency for the special case of a spin wave with a wavevector of zero ($k=0$).

Spin wave with finite wavelength values have tilt in neighboring spins relative to each other, which costs exchange energy. In this case, the magnetization will be space and wavevector dependent additionally to the time dependence. Under assumption of plane waves, the dynamic components can be written as a Fourier-series:

$$m(r, t) = \sum_k m_k(t) e^{ik \cdot r} \quad (2.25)$$

Taking the exchange field into account (see Eq. (2.20))

$$H_{ex} = \lambda_{ex} \Delta M = \lambda_{ex} \Delta (M_0 + m(r, t)) = -\lambda_{ex} k^2 m(r, t), \quad (2.26)$$

the precession frequency of spin waves with finite wavelengths is then given by the Herring-Kittel-Formula [21]:

$$f = \frac{\gamma}{2\pi} \sqrt{(H_0 + \lambda_{ex} k^2)(H_0 + \lambda_{ex} k^2 + 4\pi M_s \sin^2 \Theta_k)}, \quad (2.27)$$

where Θ_k gives the angle between the magnetization and the wavevector. From the comparison to the Kittel-Formula (2.24), it is visible that the magnetic field is increased by the additional term of $\lambda_{ex} k^2$. For the limit of $k \rightarrow 0$ the Eq. (2.27) matches the original Kittel-Formula. Therefore, spin waves with small wavevectors are usually described as *magnetostatic* spin waves. For the case of big wavevectors the exchange energy has the main contribution, thus such spin waves are *exchange* spin waves with a quadratic dispersion law.

2.3.2 Dispersion of a thin film

The Herring-Kittel-Formula is valid only in for an infinite ferromagnetic solid. In a thin film the dynamic component of the magnetization generates magnetic surface charges at the interfaces. This changes the spin-wave dispersion, especially for the spin waves with big wavelengths because of the long-range dipolar interaction. Additionally, spin-wave reflections from the surface interfaces occur, which leads to *Perpendicular Standing Spin Waves* (PSSW) and wavevector quantization in the direction along the thickness of the thin film d . In this work only the homogeneous mode $p=0$ (number of knots of the mode) will be discussed. The higher PSSW-modes lie beyond the measurement region for the samples used this work, because of exchange energy.

Spin-wave propagation in the surface plane has dispersion given by the following formula [22]:

$$f = \frac{\gamma}{2\pi} \sqrt{(H_0 + \lambda_{ex} k^2)(H_0 + \lambda_{ex} k^2 + 4\pi M_s F_{00}(\Theta, k, d))}. \quad (2.28)$$

Here, k stands for the in-plane component of the wavevector of the spin-wave. The function F_{00} is known as the *dipole matrix element* and accounts for the dipolar fields, generated by the magnetic surface charges:

$$F_{00}(\Theta, k, d) = 1 - P_{00} \cos^2 \Theta + 4\pi M_s \frac{P_{00}(k) [1 - P_{00}(k)]}{H_{eff} + \lambda_{ex} k^2} \sin^2 \Theta \quad (2.29)$$

$$\text{with} \quad P_{00}(k) = 1 - \frac{1 - e^{-k \cdot d}}{k \cdot d}. \quad (2.30)$$

The dependence on the angle Θ between the wavevector k and the static magnetization leads to a strongly anisotropic spin-wave dispersion relation. For this work of most interest is the case of $\Theta = 90^\circ$ and will be discussed next.

Magnetostatic surface mode

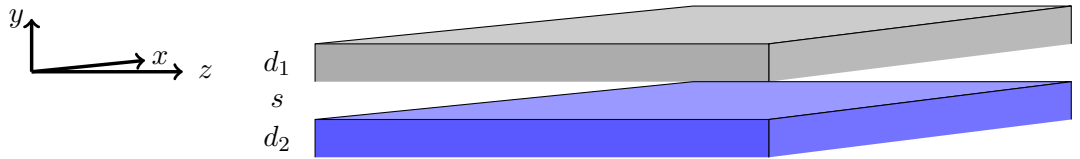
A spin-wave propagating perpendicularly to the magnetization is known as the *magnetostatic surface wave* (MSSW) or as the *Damon-Eshbach-Mode*, named after R.W. Damon and J.R. Eshbach, who were the first to calculate the dispersions of these spin-wave modes in 1961 [23]. The dispersion relation can be obtained from the Eq. (2.28) for $\Theta = 90^\circ$ if one neglects the exchange interaction:

$$f_{MSSW}(k) = \frac{\gamma}{2\pi} \sqrt{H_0(H_0 + 4\pi M_s) + (2\pi M_s)^2(1 - e^{-2k \cdot d})}. \quad (2.31)$$

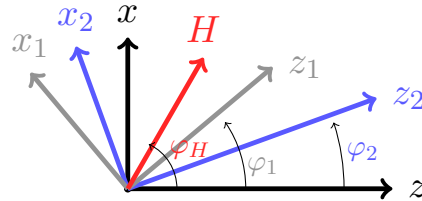
The amplitude magnetostatic surface mode is decaying exponentially over the thickness. Additionally, the MSSW has non-reciprocal property: if on one surface of the thin film the mode is propagating in a certain direction, the mode on the other surface is propagating in the opposite direction. Next, the key points of the approach to the coupled bilayer system are introduced.

2.4 Spin waves in coupled bilayers

The general handling of the two coupled multilayers does not differ much from the single layer case. Now a system, schematically shown in Fig. 2.3, is considered. The analytical approach and results presented below were provided by R.A. Gallardo, A. Roldán-Molina, and P. Landeros within the framework of a collaboration with them. Next sections shortly sum up the key points of their contribution.



(a) The bilayer system of thickness d_1 and d_2 separated by a spacer of thickness s



(b) Introduced local coordinate systems selected with respect to the equilibrium direction of the magnetization of each layer

Figure 2.3: Schema of the studied bilayer system

Starting from the same LL-equation as before, each layer has now a local coordinate system defined so that the z -direction is the equilibrium orientation of the magnetization for that layer: z_1 or z_2 respectively.

$$\frac{dM^{(i)}(r, t)}{dt} = -\gamma M^{(i)}(r, t) \times H^{e(i)}(r, t), \quad (2.32)$$

where (i) = 1 or 2 denotes the layer. In the linear regime, the magnetization can be written as $M^{(i)} = M_s^{(i)} z_i + m^{(i)}(r, t)$, and the magnetic field can be written as $H^{e(i)} = H_{z_i}^{e0(i)} + h^{e(i)}(r, t)$ (compare Eqs. (2.22)-(2.23)). Thus, the linearized equations (2.32) would lead to a total of 4 equations:

$$i\Omega m_x^{(1)}(r) = -m_{y_1}^{(1)}(r)H_{z_1}^{e0(1)} + M_s^{(1)}h_{y_1}^{e(1)}(r), \quad (2.33a)$$

$$i\Omega m_y^{(1)}(r) = m_{x_1}^{(1)}(r)H_{z_1}^{e0(1)} - M_s^{(1)}h_{x_1}^{e(1)}(r), \quad (2.33b)$$

$$i\Omega m_x^{(2)}(r) = -m_{y_2}^{(2)}(r)H_{z_2}^{e0(2)} + M_s^{(2)}h_{y_2}^{e(2)}(r), \quad (2.33c)$$

$$i\Omega m_y^{(2)}(r) = m_{x_2}^{(2)}(r)H_{z_2}^{e0(2)} - M_s^{(2)}h_{x_2}^{e(2)}(r), \quad (2.33d)$$

where the numbering denotes the layer. The further step is to assume the same plain wave form for the magnetization $m^{(i)}(r) = m^{(i)}(k)e^{ik_z z}$ and the dynamic field component $h^{e(i)}(z) = h^{e(i)}(k)e^{ik_z z}$, where k_z is the wave vector and (i) = (1), (2). Next the components $M_{z_i}^{(i)}h_{x_i}^{e(i)}(r)$ and the $M_{z_i}^{(i)}h_{y_i}^{e(i)}(r)$ can be written out explicitly:

$$M_s^{(1)}h_{x_1}^{e(1)}(r) = \left[m_{x_1}^{(1)}(k)T_{x_1} + m_{y_1}^{(1)}(k)T_{y_1} + m_{x_2}^{(2)}(k)T_{x_2} + m_{y_2}^{(2)}(k)T_{y_2} \right] e^{ik_z z}, \quad (2.34a)$$

$$M_s^{(1)}h_{y_1}^{e(1)}(r) = \left[m_{x_1}^{(1)}(k)U_{x_1} + m_{y_1}^{(1)}(k)U_{y_1} + m_{x_2}^{(2)}(k)U_{x_2} + m_{y_2}^{(2)}(k)U_{y_2} \right] e^{ik_z z}, \quad (2.34b)$$

$$M_s^{(2)}h_{x_2}^{e(2)}(r) = \left[m_{x_1}^{(1)}(k)V_{x_1} + m_{y_1}^{(1)}(k)V_{y_1} + m_{x_2}^{(2)}(k)V_{x_2} + m_{y_2}^{(2)}(k)V_{y_2} \right] e^{ik_z z}, \quad (2.34c)$$

$$M_s^{(2)}h_{y_2}^{e(2)}(r) = \left[m_{x_1}^{(1)}(k)W_{x_1} + m_{y_1}^{(1)}(k)W_{y_1} + m_{x_2}^{(2)}(k)W_{x_2} + m_{y_2}^{(2)}(k)W_{y_2} \right] e^{ik_z z}, \quad (2.34d)$$

Therefore, the equations (2.33) can be transformed into a matrix form:

$$i\Omega m(k) = \tilde{M}m(k), \quad (2.35)$$

where $m(k) = \left[m_{x_1}^{(1)}(k), m_{y_1}^{(1)}(k), m_{x_2}^{(2)}(k), m_{y_2}^{(2)}(k) \right]$ and the \tilde{M} is a 4x4 matrix of complex form.

Obviously, the complexity of the problem increased dramatically with the addition of the second layer. Nevertheless, once the effective fields are derived, the matrix can be described analytically. For that matter, the effective field contributions will be discussed next.

2.4.1 Zeeman Field

According to the in-plane geometry given by Fig. 2.3 the H^0 part of the effective magnetic field is given by:

$$H_{z_1}^{0(1)} = H \cos(\varphi_H - \varphi_1), \quad (2.36a)$$

$$H_{z_2}^{0(2)} = H \cos(\varphi_H - \varphi_2) \quad (2.36b)$$

and the relative x-projection by:

$$H_{x_1}^{0(1)} = H \sin(\varphi_H - \varphi_1), \quad (2.37a)$$

$$H_{x_2}^{0(2)} = H \sin(\varphi_H - \varphi_2). \quad (2.37b)$$

2.4.2 Uniaxial anisotropy

As the problem already becomes complex enough uniaxial anisotropy with the easy axis along x for both layers is assumed for simplicity. The energy density then reads:

$$\epsilon_u^1 = -\frac{H_u^{(1)}}{2M_s^1} \left(m_{x_1}^{(1)}(r) \cos \varphi_1 + M_s^{(1)} \sin \varphi_1 \right)^2, \quad (2.38)$$

with an analogous expression for layer 2. By considering up to second order in the spin deviation, the uniaxial anisotropy field is

$$H_{x_1}^{u0(1)} = H_u^{(1)} \cos \varphi_1 \sin \varphi_1, \quad (2.39)$$

$$H_{z_1}^{u0(1)} = H_u^{(1)} \sin^2 \varphi_1 \quad (2.40)$$

and finally

$$h_{x_1}^{u0(1)}(r) = \frac{H_u^{(1)}}{M_s^{(1)}} m_{x_1}^{(1)}(r) \cos^2 \varphi_1. \quad (2.41)$$

2.4.3 Exchange field

The exchange field is

$$H^{ex}(r) = \left(\nabla \cdot [\lambda_{ex}(r)]^2 \nabla \right) M(r), \quad (2.42)$$

where $\lambda_{ex}(r) = \sqrt{2A/\mu_0 (M_s)^2}$ is the exchange length and A is the exchange stiffness constant. The layer numbering omitted for simplicity. Considering the magnetization dynamics in the linear regime and taking into account that the exchange length is constant, the exchange field components for layer 1 are:

$$H_{z_1}^{ex0(1)} = 0, \quad (2.43)$$

$$H_{x,y}^{ex(1)}(r) = - \left[\lambda_{ex}^{(1)} \right]^2 k^2 m_{x,y}^{(1)}(r) \quad (2.44)$$

2.4.4 Dipolar fields

The dipolar fields are described by the same potential from Eq. (2.13), which already was mentioned above.

Dipolar field due to volumetric magnetic charges

The first integral of Eq. (2.13) can be evaluated analytically giving following expression for layer 1:

$$\phi_V^{(1)}(r) = i4\pi m_{x_1}^{(1)}(k) \sin \varphi_1 e^{ik \cdot r} \frac{1 - \cosh[|k| (d_1/2 + \xi_1 - y)] e^{-|k|d_1/2}}{|k|^2}, \quad (2.45)$$

where coordinate $\xi_1 = d_2 + s$ and coordinate y is measured from the bottom of the second layer. Next, the dynamic dipolar field components can be obtained from the equation (2.9):

$$h_z^{V(1)}(z) = 4\pi m_{x_1}^{(1)}(k_z) \sin \varphi_1 \left[1 - \cosh[|k_z| (d_1/2 + \xi_1 - y)] e^{-|k_z|d_1/2} \right] e^{ik_z z}, \quad (2.46a)$$

$$h_y^{V(1)}(z) = -i4\pi m_{x_1}^{(1)}(k_z) k_z \sin \varphi_1 \frac{\sinh[|k_z| (d_1/2 + \xi_1 - y)] e^{-|k_z|d_1/2}}{|k_z|} e^{ik_z z}. \quad (2.46b)$$

The equations for the layer 2 are identical with the difference in $\xi_2 = 0$. Now, the fields are averaged along the thickness d_1 , so $h_y^{V(1)}(z) = 0$ and

$$h_z^{V(1)}(z) = 4\pi m_{x_1}^{(1)}(k_z) \left[1 - \frac{2 \sinh[|k_z|d_1/2] e^{-|k_z|d_1/2}}{d_1|k_z|} \right] \sin \varphi_1 e^{ik_z z} \quad (2.47)$$

Additionally to that, the dipolar fields acting from one layer to another should be accounted for. These calculations result in the following expression:

$$h_z^{V(2_1)}(z) = 4\pi m_{x_1}^{(1)}(k_z) \sin \varphi_1 e^{ik_z z} \sinh[|k_z|(d_1/2)] \frac{2 \sinh[|k_z|d_2/2] e^{|k_z|d_2/2}}{d_2|k_z|} e^{-|k|(d_1/2+\xi_1)}, \quad (2.48)$$

where the 2_1 notation means a field is generated by system 1 but acting in layer 2. The $h_y^{V(2_1)}(z)$ component has a similar form.

Dipolar field due to surface magnetic charges

The second integral of the equation (2.13) gives the magnetic potential generated by the surface charges. It is given by

$$\phi_S^{(1)}(r) = 2\pi m_{y_1}^{(1)}(k) \sinh[|k|(y - d_1/2 - \xi_1)] \frac{e^{-|k|d_1/2}}{|k|} e^{ik \cdot r} \quad (2.49)$$

for layer 1. Then, calculating the dynamic dipolar components from Eq. (2.46) and averaging along the thickness results in $h_z^{S(1)}(z) = 0$ and

$$h_y^{S(1)}(z) = -4\pi m_{y_1}^{(1)}(k_z) \frac{2 \sinh[|k_z|d_1/2] e^{-|k_z|d_1/2}}{d_1|k_z|} e^{ik_z z}. \quad (2.50)$$

Similarly to the case for the volumetric charges the dipolar fields generated in one layer by the other one are given by:

$$h_y^{S(2_1)} = 4\pi m_{y_1}^{(1)} \sinh[|k_z|(d_1/2)] \frac{2 \sinh[|k_z|d_2/2] e^{|k_z|d_2/2}}{d_2|k_z|} e^{-|k|(d_1/2 + \xi_1)} e^{ik_z z}. \quad (2.51)$$

2.4.5 Interlayer Exchange Interaction

The interlayer exchange energy density is given by

$$\epsilon_{iEx} = -\frac{J}{M_s^{(1)} M_s^{(2)}} \left[M^{(1)}(r) \cdot M^{(2)}(r) \right]. \quad (2.52)$$

Taking into account, that the magnetization can be written as $M^{(i)}(r) = M_s^{(i)} z_i + m_{x_i}^{(i)} x_i + m_{y_i}^{(i)} y_i$ the components of the interlayer exchange field are given by

$$H_{z_1}^{iEx0(1)}(z) = \frac{J}{d_1 M_s^{(1)}} \cos(\varphi_2 - \varphi_1), \quad (2.53)$$

$$H_{x_1}^{iEx0(1)}(z) = \frac{J}{d_1 M_s^{(1)}} \sin(\varphi_2 - \varphi_1), \quad (2.54)$$

for the first layer. Additionally, the dynamic components are:

$$h_{y_1}^{iEx0(1)}(z) = \frac{J}{d_1 M_s^{(1)} M_s^{(2)}} m_{y_2}^{(2)}(k_z) e^{ik_z z}, \quad (2.55)$$

and

$$h_{x_1}^{iEx0(1)}(z) = \frac{J}{d_1 M_s^{(1)} M_s^{(2)}} m_{x_2}^{(2)}(k_z) \cos(\varphi_2 - \varphi_1) e^{ik_z z}. \quad (2.56)$$

The second layer obviously has identical field components, which are omitted for the sake of simplicity. As all of the field components are now described the next step is to include them into the equation of motion (2.35). Next sections will address the arising physical effects for the coupled bilayer system.

2.5 Theoretical Predictions

The spin waves spectra of two bilayers configurations have been calculated by T. Schneider. The first case is a Py/Py bilayer system where Py stands for Permalloy ($Ni_{80}Fe_{20}$). Each layer is 6 nm in thickness and the layers have a spacing Cu layer of 5 nm in between them. The bottom (or the layer (2)) is exchange-biased. Both of the layers are identical and typical

magnetic parameters for Py were used, i.e., a saturation magnetization $M_s^{(1,2)} = 800$ kA/m and $A_{Py}^{ex} = 13$ pJ/m. Second case is a CoFeB/CoFeB bilayer system where each layer is again identical with $M_s^{(1,2)} = 1250$ kA/m and $A^{ex} = 15$ pJ/m. Here the layers are both 10 nm in thickness and are separated by a thin Ir layer of 0.45 nm wherefore the interlayer exchange is of more importance compared to the first case.

First, it is important to understand that the bilayer system can be in two unique states:

1. Magnetization vectors of the layers are collinear, e.g. ferromagnetic state
2. Magnetization vectors of the layers are antiparallel, e.g. antiferromagnetic state

The case #1 is in its physics not much different from a single thin film case. There, the dispersion curves are symmetric, $\omega(k) = \omega(-k)$, displaying *reciprocal* behaviour of two counterpropagating spin waves. Case #2, however, leads to interesting *non-reciprocal* effects ($\omega(k) \neq \omega(-k)$). Fig. 2.4 presents the obtained dispersion relation curves for both of the bilayer systems in the case of antiparallel alignment of the layers.

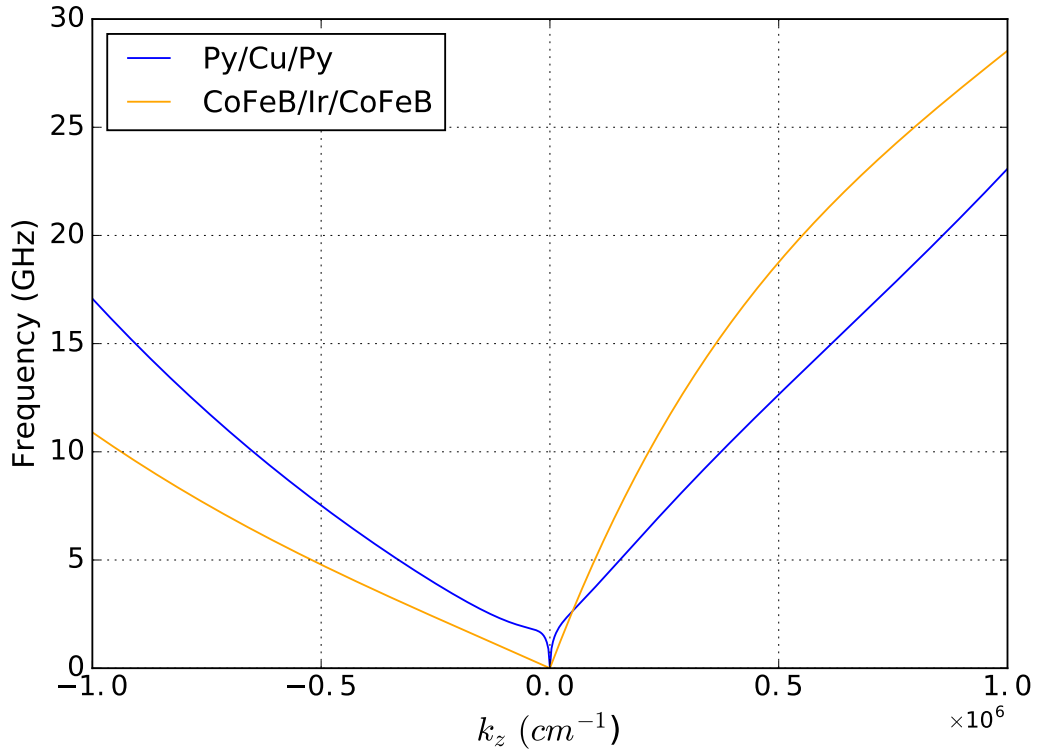


Figure 2.4: Dispersion Relation curves for the two bilayer systems, calculations of T. Schneider

From the Fig. 2.4 it is clearly visible, that the spin-wave propagation is non-reciprocal with respect to the k_z -direction. For example, for the wavevector of $1.67 \cdot 10^5$ cm^{-1} the difference in the frequency Δf of the counterpropagating spin waves for the Py/Cu/Py system is equal to 2.4 GHz. The frequency difference plots are illustrated in Fig. 2.5.

Next, assuming the same theory and an excitation with a point source, the isofrequency curves $f_{const} = f(k)$ can be obtained. Isofrequency curves serve as a good method of visualization of the dispersion of a material. The isofrequency curves show all allowed wavevectors of the system and their corresponding frequencies. For the Py/Cy/Py the resulting isofrequency curves for 3, 4, and 5 GHz are shown in Fig. 2.6. Note, that the group velocity $v_g = \frac{\partial \omega}{\partial k} \propto \nabla_k \omega(k)$ is always normal to the isofrequency line. Hence, when the curvature

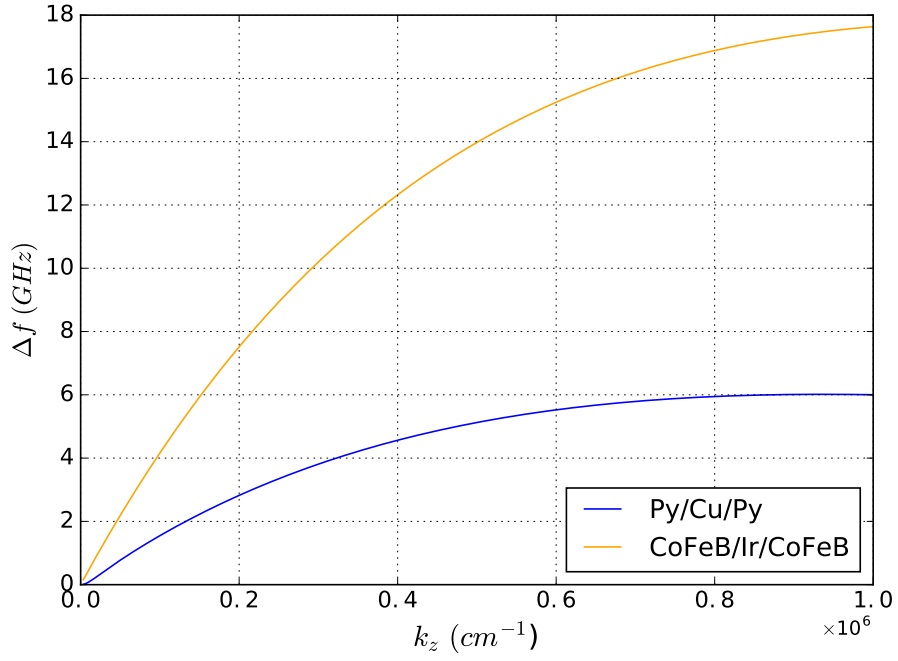


Figure 2.5: Frequency difference of two counterpropagating waves as a function of the wavevector

of an isofrequency line has an extreme value (is zero or changes sign) for a certain interval of wavevectors the group velocity will be pointing in the same direction. The resulting interference pattern of these spin waves will form the so-called *caustic beams*.

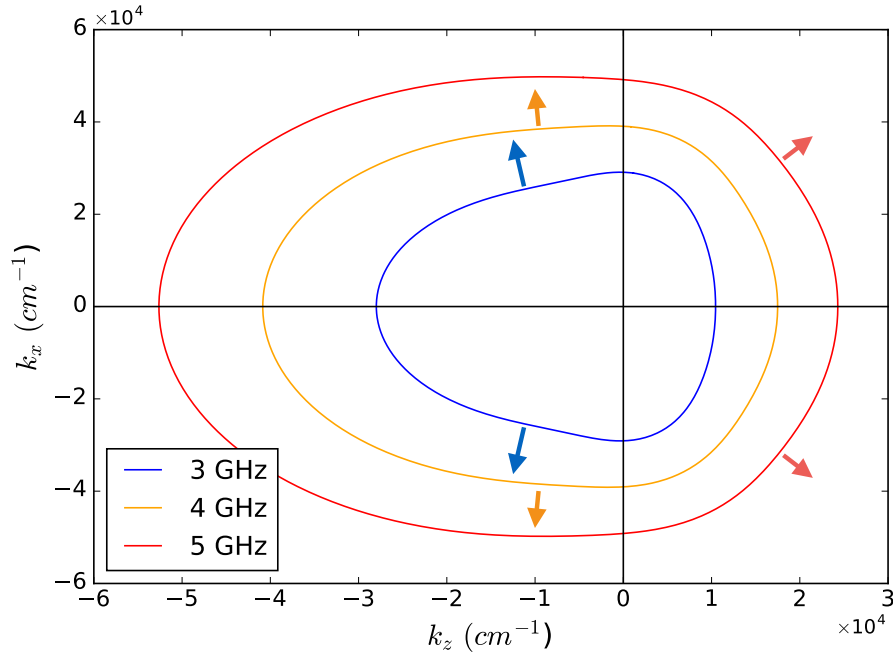


Figure 2.6: Isofrequency curves for the Py/Cu/Py system, arrows indicate the direction of the group velocity, calculations of T. Schneider

As the group velocity is $v_g = \frac{\partial \omega}{\partial k}$, the angle of the caustic beams is defined as

$$\theta = \arctan\left(\frac{\partial \omega / \partial k_x}{\partial \omega / \partial k_z}\right) = \arctan\left(\frac{\partial k_z}{\partial k_x}\right). \quad (2.57)$$

Fig. 2.7 shows the difference in the caustic beam angles between the two isofrequency curves of 3 and 4 GHz.

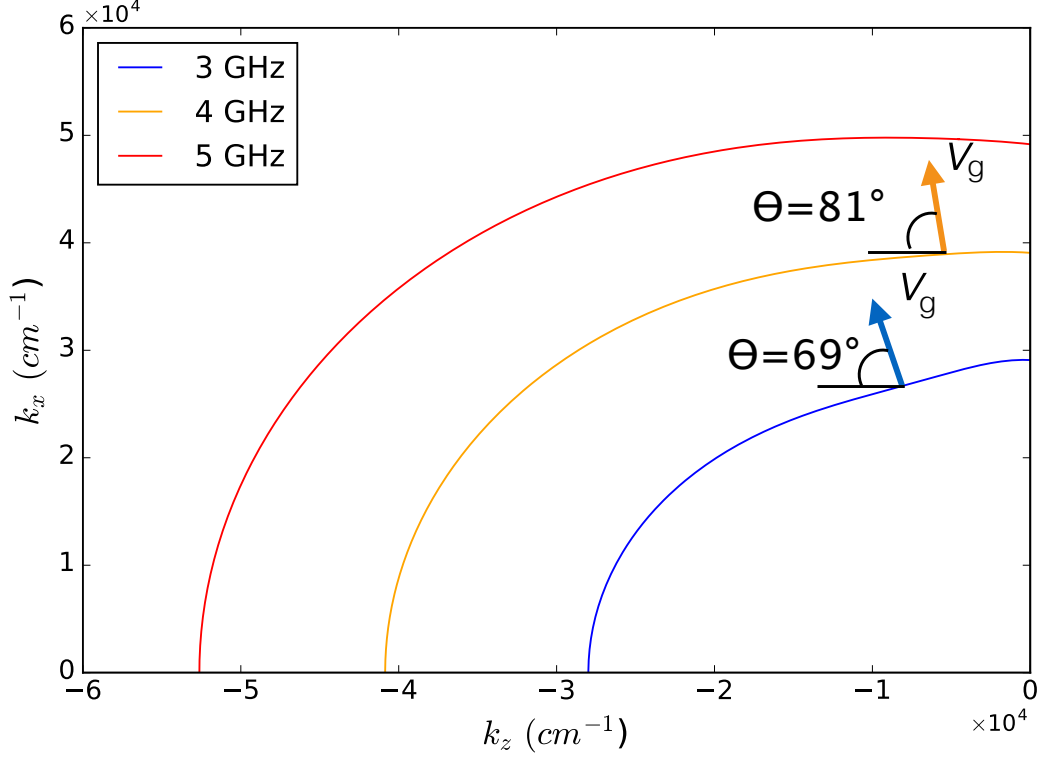


Figure 2.7: Difference in angles of the possible caustic beams for 3 and 4 GHz, arrows indicate the direction of the group velocity, calculations of T. Schneider

3 Experimental Setup

During the work on this thesis spin waves were investigated by means of micro-focused Brillouin Light Scattering Microscopy as well as a setup for traditional Brillouin Light Scattering was build up. The fundamentals of these methods are discussed in this chapter.

3.1 Brillouin-Light-Scattering (BLS)

The foundation of Brillouin-Light-Scattering (BLS) is the inelastic scattering of monochromatic light with collective excitations of a physical medium - phonons being the quantum counterpart of acoustic excitations and magnons being the quantum counterpart of spin waves.

A typical optical experiment to investigate the collective excitation of a physical medium is described by Fig. 3.1.

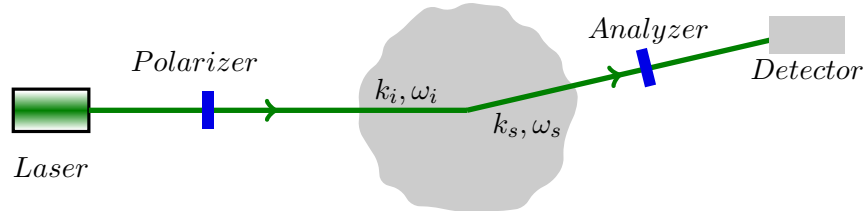


Figure 3.1: Schema of typical scattering experiment

In the particle model, two processes are possible during scattering to satisfy the energy and momentum conservation.

$$\hbar k_i = \hbar k_s \pm \hbar Q, \quad (3.1)$$

$$\hbar \omega_i = \hbar \omega_s \pm \hbar \omega. \quad (3.2)$$

A *Stokes process* is defined by the incident photon losing energy and momentum to create an excitation in the medium ("-" sign in Eq. (3.1) and (3.2)). An *anti-Stokes process* is defined by the gain of energy and momentum of the incident photon because of an annihilation of the excitation in the medium ("+" sign in Eq. (3.1) and (3.2)). This is schematically illustrated in Fig. 3.2.

Following these conditions of energy and momentum conservation, it is clear, that it is possible to determine the frequency as well as the wave-vector if the respective values of the incoming and scattered light are known. Considering the fact that the phase velocity

3 Experimental Setup



Figure 3.2: Two possible scattering processes; Photons are marked with green and magnons with red color respectively

of the spin waves is quite low compared to the speed of light the frequency shifts with the same wave vectors of light and magnons are small and typically lie in the GHz range. This demands for a very high energy resolution and contrast of the analyzing equipment. Next sections will describe the interferometry equipment used to achieve this resolution.

Regarding the wave vector resolution, a comment needs to be made. The momentum conservation is valid only in a translationally invariant system. For a thin film system, this means that only component of the wave vector parallel to the film plane $k_{||}$ is conserved. For this reason, the equations (3.1) must be modified to include only the projections to the film plane instead of full wave vectors of the incident and scattered light. If one then manages to fix the incident angle of light (see Fig. 3.3) with respect to the film surface precise enough it is possible to realize a wave vector selective Brillouin Light Scattering spectroscopy [24] via the following relation:

$$Q = pk_i \cos(\theta) = p \frac{2\pi}{\lambda_{Laser}} \cos(\theta) \quad (3.3)$$

The p factor describes the two common scattering geometries used for such experiments. For transparent mediums usually a *forward* scattering geometry is realized. Here the laser light is focused on the sample by a lens with a very large focal length and after that, the scattered light is gathered by another objective. As only one full wave vector of the incident light can be transferred in such geometry the factor in the Eq. (3.3) must be set to $p = 1$.

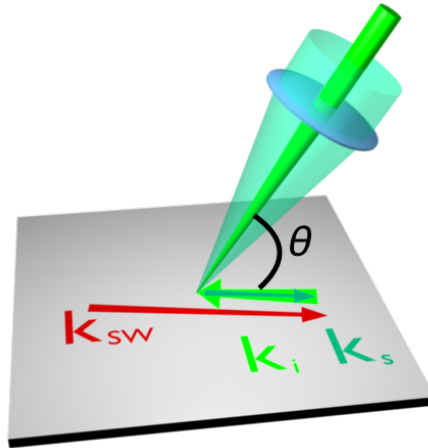


Figure 3.3: BLS spectroscopy in backward scattering geometry. The focused, as well as the scattered light, are gathered by the same lens, automatically leading to wavevector selectivity. Image from [15]

The investigation of non-transparent materials or excitations with large wave vector demands the choice of the *backward* scattering geometry, which was also used for all experiments in this work. In this geometry, the light is focused onto the sample by a camera objective with a large focal distance. Then the scattered light is gathered with the same camera objective in backward scattering. Considering the fact that now the lens is collecting the light under the same angle it was falling onto the sample hereby automatically wave vector selectivity is realized. In the extreme case of $\theta = 0^\circ$ (glazing incidence), the double of the incident light wave vector is transferred to the sample. Therefore the factor p in the Eq. (3.3) can be set to 2 for the backscattering geometry. For the solid-state laser of wavelength $\lambda_{\text{Laser}} = 532 \text{ nm}$ used in this work this sets the maximum range of available wave vectors $k_{\text{max}} = \frac{4\pi}{\lambda_{\text{Laser}}} = 2,36 \cdot 10^5 \text{ cm}^{-1}$. The different incident angles of light are usually achieved through a goniometer stage so the sample is then rotated through the focus point.

3.1.1 Fabry-Pérot Interferometer

A very common and highly precise method of frequency measurement relies on multibeam interference. In this work, this is realized on the base of a Fabry-Pérot-Interferometer(FPI). An FPI consists of a pair of one-side highly reflective and very flat mirrors mounted parallel to each other at a variable distance. Upon entering of light multiple reflections occur leading to multibeam interference. Fig. 3.4 shows the multiple reflections of the light under a non zero angle of incidence only for clarity. In reality, the light is falling perpendicular to the interferometer. For a set distance d between the mirrors, this multibeam interference results in the transmission of light only if the interfering beams have a certain phase difference between each other. The optical path difference Δs of two beams in the case of perpendicular incidence is given by $\Delta s = 2nd$, where n describes the refractive index of the medium between the two plates of the FPI. As for this work, the FPI is mostly filled with air the n can be set to 1 and will not be discussed in further expressions.

Knowing the optical path difference one can easily derive the resulting phase difference $\Delta\phi$ between the two interfering beams of the wavelength λ :

$$\Delta\phi = \frac{2\pi\Delta s}{\lambda} = \frac{4\pi d}{\lambda} \quad (3.4)$$

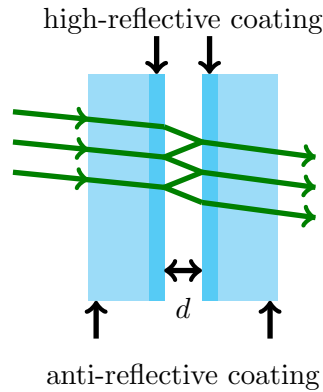


Figure 3.4: Schematic illustration of a single Fabry-Pérot-Interferometer consisting of a pair of one-side highly reflective plates. The green arrows depict the multiple passing of the light beams under a nonzero angle of incidence.

To be able to tell for which phase difference constructive interference is occurring the transmission function of the FPI needs to be taken into account. The transmission function is given by the ratio of the transmitted (I_T) to the incoming (I_0) light intensity and can be calculated with the *Airy-Formula* [25]:

$$T = \frac{I_T}{I_0} = \frac{1}{1 + F \sin^2(\Delta\phi/2)} \quad (3.5)$$

The Finesse F describes the relation between the distance separating two transmission maxima and their Full Width at Half Maximum (FWHM) values. Therefore it mainly describes the resolution capabilities of the FPI and depends only on the mirrors reflectivity R :

$$F = \frac{4R}{(1 - R)^2} \quad (3.6)$$

An increase of the mirror reflectivity leads to a higher finesse of the FPI, which results in a bigger ratio between maximal and minimal transmission. This means an increase of the contrast of the FPI with higher finesse. In addition to that, as finesse describes the distance between two transmission maxima in relation to their width, it, therefore, defines the resolution of the FPI which also is better with higher values of the finesse.

The transmission function defined by Eq. (3.5) is periodic in the phase difference $\Delta\phi$ and has a maximum when the phase difference $\Delta\phi = 2m\pi$, where $m \in \mathbb{N}$. Combining that with the Eq. (3.4) one can easily determine that the transmission is maximal for mirror distances which are multiples of the half-wavelength: $d = m\lambda/2$. FPI can be seen as an optical bandpass for this reason. It can be used for measurements of transmission as a function of mirror distance, which would give to access to frequency information.

If a beam of reference wavelength λ_r passes through the FPI at a certain mirror distance d_r another beam of wavelength λ will be transmitted upon the change to another mirror distance $d_r + \Delta d$ which for our case describes the wavelength of investigated magnons. This wavelength can be calculated as follows:

$$\lambda(\Delta d) = \lambda_r \left(1 + \frac{\Delta d}{d_r} \right) \quad (3.7)$$

Having this formula the frequency difference between the two transmitted wavelengths λ_r and λ reads as:

$$\Delta\nu = |\nu_r - \nu| = \left| \frac{c}{\lambda_r} \left(1 - \frac{1}{1 + \frac{\Delta d}{d_r}} \right) \right| = \left| \frac{c}{\lambda_r} \frac{\Delta d}{d_r + \Delta d} \right| \approx \left| \frac{c}{\lambda_r} \frac{\Delta d}{d_r} \right| \quad (3.8)$$

The last approximation made in Eq. (3.8) is justified because the typical changes of the mirror distance Δd are on the order of magnitude of the wavelength itself and the set distance d_r for the reference measurement is varied between 0.3 to 15 mm. Therefore the frequency difference is linear in the mirror distance variation Δd with good approximation. Measuring the mirror distance variation in comparison to the set working distance allows for derivation of the frequencies of the spin waves. Modern FPIs achieve extremely precise shifts in the mirror distance in the range of ångströms with piezoelectric actuators. The frequency shifts can be calculated back from the respective voltages applied to the actuators. For the reference wavelength, the 532 nm line of a solid-state laser is used.

Another important aspect can be derived from Eq. (3.8). The distance between two successive transmission maxima is given by the mirror distance $\Delta d = \lambda_r/2$ and is known as the *Free Spectral Range (FSR)*:

$$FSR [GHz] = \Delta\nu \left(\frac{\lambda_r}{2} \right) \approx \frac{c}{2d_r} \approx \frac{150}{d_r [mm]} \quad (3.9)$$

This connection between the FSR and the working distance of mirrors decides the spectral resolution of an FPI. The available during measurement spectral range decreases upon increase of the working mirror distance d_r . As the resolution is dictated by the finesse the

distance between two successive transmission maxima as well as their FWHM is constant in the units of FSR. Therefore the spectral resolution is higher the further the mirrors are from each other.

3.1.2 Tandem-Fabry-Pérot-Interferometer

As already stated above the transmission maxima of a single FPI repeat themselves each time the mirror distance is equal to the half of the wavelength. Fig. 3.5 (a) shows a spectrum detected by a single FPI. Next, to the central transmission order n the neighboring transmission maxima, as well as the measured magnonic signals, are visible.

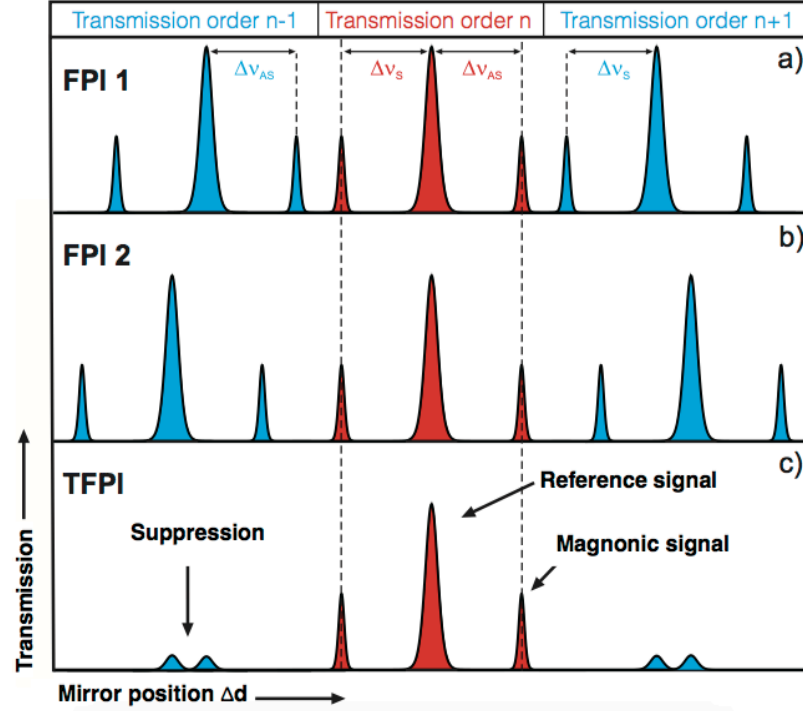


Figure 3.5: Transmission spectra for clarification of the functionality of a Tandem-Fabry-Pérot Interferometers. Image from [15]

However, a question arises upon analysis of this spectrum if the measured signal is coming from a Stokes-process of the central transmission order n or if it indeed belongs to the Anti-Stokes process of the $n-1$ transmission order. To overcome this problem a Tandem-Fabry-Pérot-Interferometer developed by J. R. Sandercock [26] was used in this work. Following the name, the device obviously consists of two FPIs with their optical axes under an angle α between them. Fig. 3.6 displays the schematical setup of such a TFPI. For each of the two FPIs, the right glass mirror plate is mounted on a movable stage which can be displaced mechanically to set the working distance d_r . In addition to that, the stage can be shifted by piezoelectric actuators with very high precision. If the stage is moved by Δd the mirror distance for the 1st FPI changes by Δd but the mirror distance for the 2nd FPI changes by a smaller value of $\Delta d \cos(\alpha)$. Therefore the distance between the two transmission maxima for the FPI 2 is higher (see Fig. 3.5 (b)).

For the light to pass through the TFPI the transmission condition given by Eq. (3.5) must be fulfilled for both etalons. For the central transmission order, the synchronization of the two etalons can be realized by piezoelectric actuators, which allow for adjustment of the mirror distance of the FPI 2 separately from FPI 1. The higher order transmission maxima with their respective Stokes and anti-Stokes lines does not occur simultaneously, however.

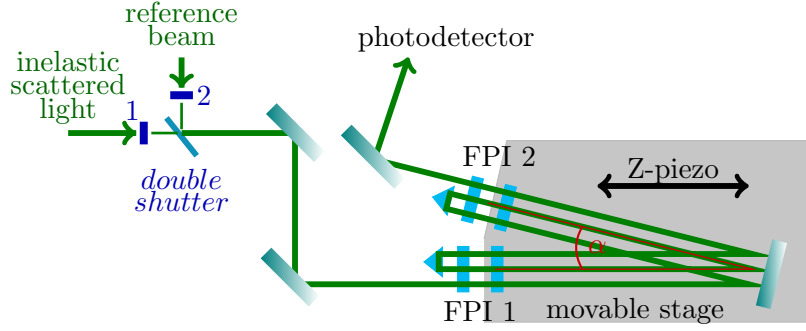


Figure 3.6: Operation scheme of a Tandem-Fabry-Pérot-Interferometer. According to the current state of the *double shutter* either the light scattered from the sample or the reference beam are passing through it. Light is passing each of the FPIs 3 times on the way to the photodetector. The optical axes of the two FPIs are put under a certain angle α between them, resulting in suppression of the higher transmission orders

As the transmission of the TFPI is the product of the transmissions of the two single FPIs these higher order peaks are now highly suppressed. Therefore the TFPI allows for clear ordering of the measured spin-wave signals to the central transmission order.

Because of very low scattering cross section of photon-magnon scattering processes elastically scattered light has usually intensity higher than the inelastically scattered by a factor of around $10^{15} - 10^{20}$. For this reason, extremely high contrast is needed to resolve the inelastically scattered light from the elastically scattered light. The needed contrast is reached as the light is passing each of the etalons 3 times respectively before it goes to the photodetector. This is why usually about a (3+3)-Tandem-Fabry-Pérot-Interferometer is spoken. The high finesse of such interferometer is guaranteed by the accordingly big reflectivity of the mirrors. For light to have many reflections between the mirrors extremely high surface quality and parallelity of mirrors is very important.

During this work, a software program "Tandem-Fabry-Pérot-Data Aquisition Software 4" (TFPDAS4) developed by H. Schultheiß via the *National Instruments Labview* programming environment was used. This program is a further development of the TFPDAS3 program made by B. Hillebrands [27] and allows for space-resolved measurements under variation of up to 3 external parameters, for example of external magnetic field, excitation frequency, and the microwave power.

One can see from the Fig. 3.6 that not only the light coming from the sample is coupled into the TFPI but also a reference beam. This has the following reasoning behind it: in a backward scattering experiment, the objective collects not only the light scattered on magnons but also all other inelastic scattered light which is high in intensity and could damage the sensitive photodetector. Therefore on the entrance of the TFPI a *double shutter* is placed. Whenever the mirror distance of the TFPI fulfills the transmission condition of the inelastically scattered light the shutter 1 is closed and the shutter 2 of the reference beam is opened (in Fig. 3.6 schematically in blue). The reference beam is used as a frequency normal and is sampled with low enough intensity from the initial laser beam before it hits the sample. At all other times, the light inelastically scattered on magnons is let through the interferometer.

The choice of the focusing optics, as well as realization of the sample positioning system, lead to two possible BLS setups in which the TFPI is used as the main analyzing unit:

1. Conventional BLS
2. Micro-focused BLS

Next sections will be dedicated to the explanation of these setups.

3.2 Conventional Brillouin Light Scattering

A conventional Brillouin Light Scattering Spectroscopy setup resides fundamentally in the wave vector selectivity, possibility of which was introduced at the start of this chapter. As the non-reciprocal properties for the multilayer systems investigated in this thesis mainly result in the different dispersions of the spin waves for the positive and negative wave vectors, a conventional BLS setup was naturally chosen to measure these effects. As the laboratory did not have a functional conventional BLS setup, I assembled it alongside the already existing micro-focused BLS setup on the same optical table. The principle scheme of the constructed conventional BLS is presented by the Fig. 3.7.

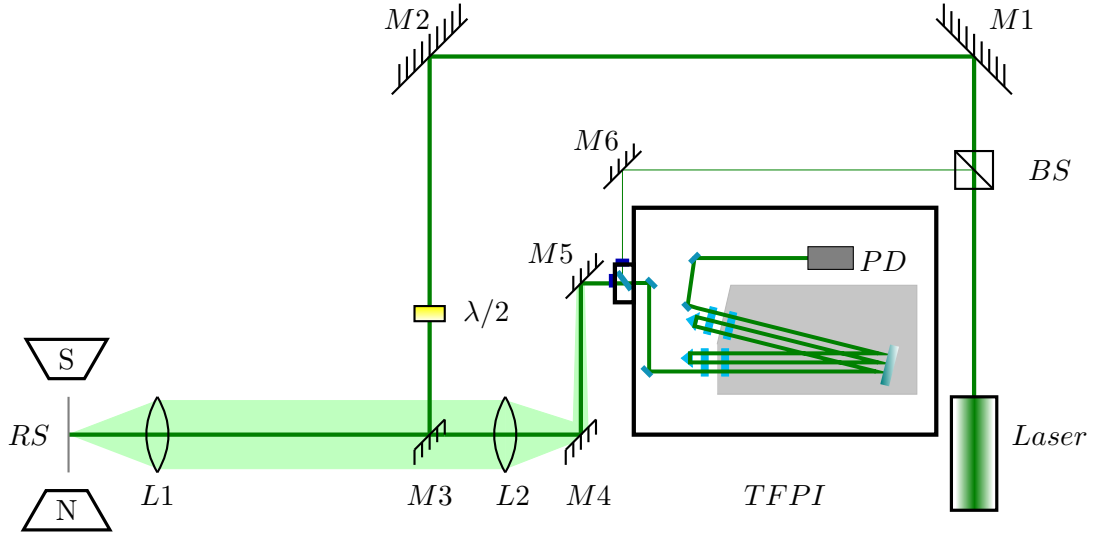
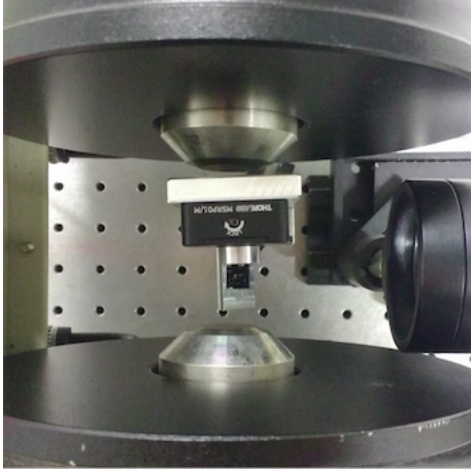


Figure 3.7: Conventional BLS setup; *BS* — Beam Splitter, *RS* — Rotary Stage, *PD* — Photo Detector, numbered *M* – mirrors used in the setup

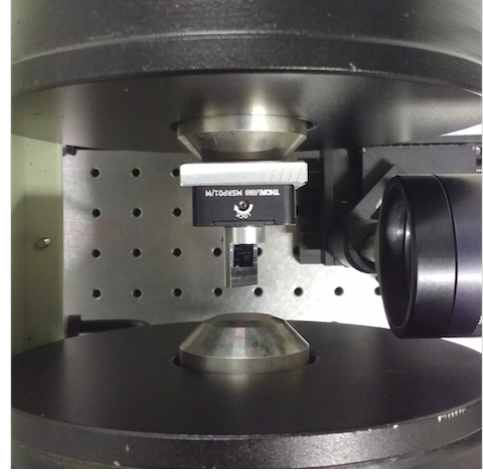
The beam comes out of a 532 nm wavelength solid-state laser. On its way to the sample, it passes a beam splitter. One part of the beam carrying 10% of the original beam intensity is guided directly to the interferometer and used as the reference beam for stabilization of the TFPI and the zero of frequency. The other part of the beam is passing a $\lambda/2$ plate before reaching the mirror M3 directing the light to the sample mounted on a 360° rotary stage. This is very important due to the fact that the light rotates its polarization by 90° upon scattering on magnons. As the used in this work TFPI is polarization sensitive it is crucial to select the polarization of the incoming light so it is then able to be detected after the scattering occurs. For focusing of the light onto the sample a lens of 75 mm focal distance is used (L1) and the magnetic field is applied via an electromagnet capable of reaching a maximum field 200 mT in strength. Maximum available laser power before the focusing lens is 39 mW.

As conventional BLS is sensitive on the incident angle of the laser light measurements under different incident angles can be used to map the dispersion relation of SW for a specific film. The measurement procedure is straightforward: focus the laser beam to the sample at a set angle of incidence and collect the BLS spectrum and then repeat for next angle. The measured signal is obviously dependent on good focusing as well as on film quality. For tests, a 30 nm thick reference Py film was used, because it was giving a good signal to noise ratio in short amount of time. The signals from the main samples of the project were a lot weaker compared to the reference film and therefore required a lot of careful focusing as the

build setup is completely manual in that sense. The only way of checking if the current lens position is giving a well focused beam is to place the lens in roughly 75 mm distance from the sample and then to accumulate the spectrum. Then the lens can be moved by a micrometer screw and the spectrum can be recorded again. In such way, step-by-step the signal can be improved and the best lens position for the current angle of incidence can be found. For each angle of incidence, the *Stokes* and *anti-Stokes* peaks of the full resulting BLS spectra are then fitted by a Lorentzian curve and should have the same frequency if the investigated film does not have non-reciprocity.



(a) Exaggerated example of incorrect alignment of the sample holder with respect to the magnet



(b) Example of correct alignment of the sample holder with respect to the magnet

Figure 3.8: Importance of a proper sample holder alignment

To be able to measure non-reciprocity one must first make sure that the experimental setup gives correct results on reference samples. An example of a measured DR for a 30 nm thick Py film is given in Fig. 3.9a. Even slight misplacement of the sample holder with respect to the magnet and incident light gives rise to incorrect results showing non-reciprocal DR of SW in the same reference film (Fig. 3.9b). This effect comes from the sample not being parallel with respect to the magnet. An exaggerated example of such sample holder misalignment is illustrated by Fig. 3.8a. In such case, the sample has a field which also has an out of plane component which significantly changes the frequency of the spin-wave spectrum and therefore the dispersion relation is non-symmetric for positive and negative angles of incidence.

To identify such problems conventional BLS setup working condition can be tested with Plexiglas. Plexiglas is nothing other than Poly(methyl-methacrylate) or acrylic glass. Phonons of the glass have much higher scattering cross-section compared to magnons giving more than 50 times higher signal output in the same experiment. This allows for simple test measurements verifying if the alignment of the setup is correct. For a properly aligned system both *Stokes* and *anti-Stokes* peaks should have the same frequency as well as intensity (see Fig. 3.10). For the illustrated spectrum the frequency difference is only 90 MHz which on the same order as the frequency error of the TFPI at 5 mm etalon distance.

3.3 Micro-focused Brillouin Light Scattering (μ BLS)

In the conventional BLS the used lenses have high focal distance and focus the incident light under a very small spatial angle onto the sample. Although providing wave vector selectivity

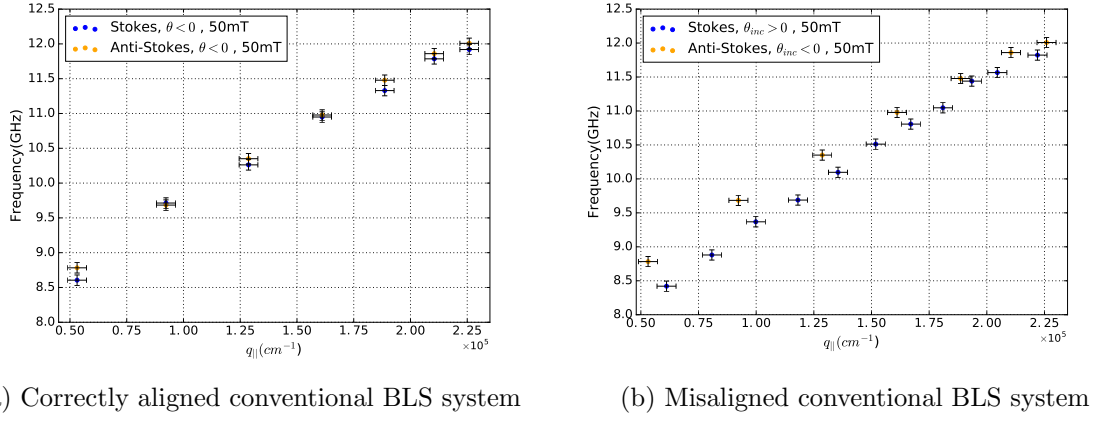


Figure 3.9: Two measured dispersion relations for a 30 nm thick Py reference film at 50 mT of the external field

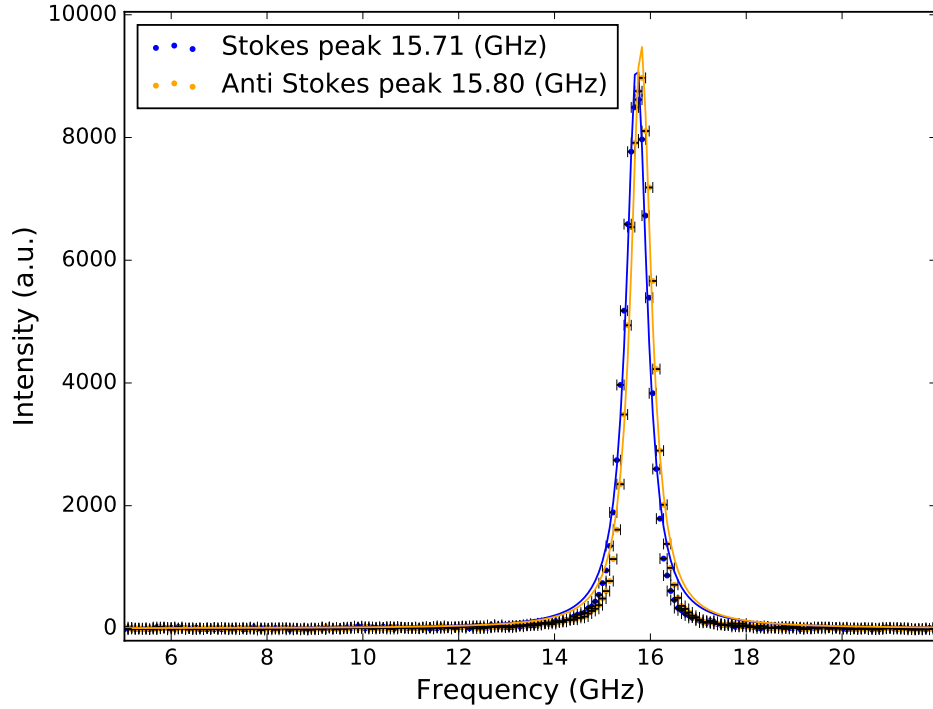


Figure 3.10: BLS spectrum of Plexiglas

this limits the space resolution dramatically. Looking at the formula for the focus diameter w :

$$w \simeq 1,22 \frac{f \cdot \lambda}{w_0}, \quad (3.10)$$

as $w \simeq f \cdot \theta$ and $\theta \approx \lambda/w_0$ - Rayleigh criterion [28].

For the 532 nm line of the laser used in the experiment, the beam diameter is approximately $w_0 = 2$ mm. Considering a typical working distance of $f = 7.5$ cm this results in the focus diameter of 23 μ m for the conventional BLS. This makes it impossible for space-resolved investigation of structures in nano- or micrometer range except for cases of ordered grids of identical elements.

3 Experimental Setup

To raise the spatial resolution for the purpose of Brillouin-Light Scattering microscopy a microscope objective with high numerical aperture and a working distance of $f = 4$ mm is used. This objective has an entry opening of 3 mm in diameter which is fully illuminated. The spatial resolution for this case can be improved to almost 250 nm [15]. However, in this case, the light does not fall onto the sample under a fixed angle θ . It is covering a spatial angle of half opening angle $\beta = \arcsin(NA)$ (NA - numerical aperture). For the used objective $NA = 0,75$ and therefore results in a spatial angle of the opening $2\beta = 97,2^\circ$. According to the Eq. (3.3) the maximum momentum transfer results in $k_{max} = 1,7 \cdot 10^5 \text{ cm}^{-1}$. The wave vector selectivity is lost, however, because the microscope objective is now gathering the scattered light in the whole spatial angle which is shown in Fig. 3.11.

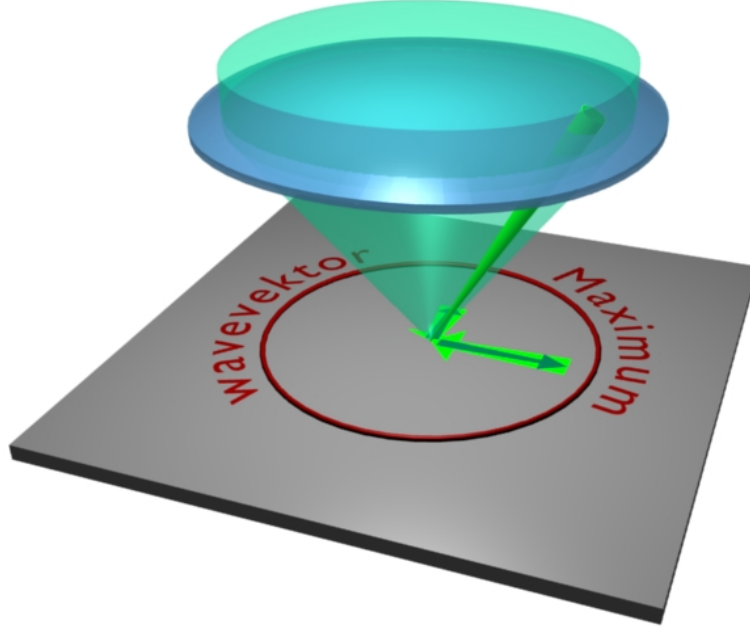


Figure 3.11: Illustration of the scattering geometry for a BLS-microscope.
Image from [15]

As the microscope objective must be fully illuminated the 2 mm wide initial beam of the laser must be expanded. The setup of the BLS microscope has additional differences compared to the conventional BLS setup. The schematics of the used in this work BLS microscope are illustrated by Fig. 3.12.

First, the beam coming out of the laser is expanded on passing through a telescope to the 3 mm diameter. This allows for full illumination of the microscope objective later and also improves the beam parallelism. On the way to the sample the light is passing two 50:50 beam splitters and then focused by an "LD EC Epilan-Neofluar" objective (magnification: 100x, numerical aperture: 0.75, working distance: 4mm). The inelastically scattered light was then gathered back by the same objective and guided to the TFPI with a 50:50 beam splitter. The part of the scattered light, containing relevant information is filtered from the strong on intensity elastically scattered light by the means of the *double shutter* already described before. The illumination with a red led allows for imaging of the current position of the focused laser with respect to the sample via a CCD-camera. Software image recognition techniques allow for best focusing and stabilization of the position during the measurements.

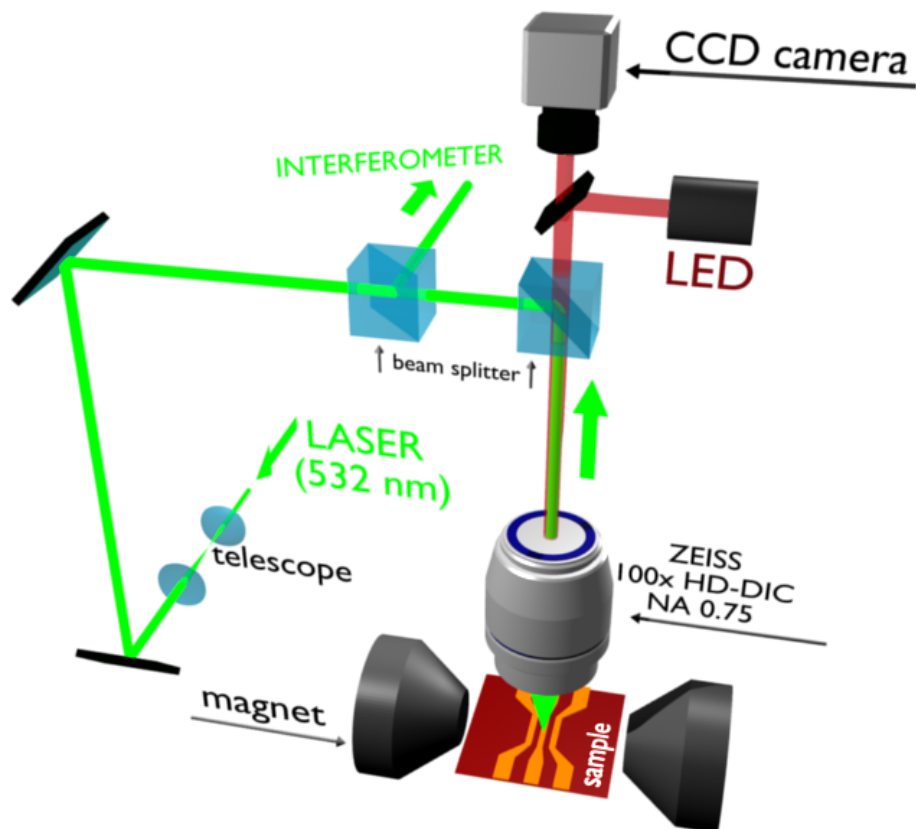


Figure 3.12: 3D-model of the micro-BLS setup.
Image: courtesy of H.Schultheiß

4 Results and Discussion

This chapter is dedicated to the presentation of experiments, which were carried out during this work, and to the discussion of their results. The chapter is organized into three major blocks: an overview of samples, conventional BLS measurements of thermally excited spin waves in these samples and finally μ BLS measurements on the transport of spin waves.

4.1 Samples overview

The samples measured by the conventional BLS and the μ BLS consist of multi-layers of thin films grown on Si/SiO_2 substrate. The samples always include two ferromagnetic layers separated by a non-magnetic material. These ferromagnetic layers are coupled via:

1. Exchange bias, which is set by an IrMn antiferromagnetic layer
2. Ruderman-Kittel-Kasuya -Yoshida interaction (RKKY interaction), which is induced by a thin spacing layer.

The detailed layer composition for each measured sample is summarized in Fig. 4.1.

As the first two samples are coupled via exchange bias a comment needs to be made about their preparation. The exchange bias can be set either with external field application during the deposition or with a field-cooling procedure. Both approaches have their influence on the sample quality. According to P. Arekapudi, who did the actual composition of the samples at the TU Chemnitz, a deposition in field makes the films not so smooth as without the field, which supposedly can lead to higher damping. Annealing can cause diffusion of the spacing layer into the ferromagnetic layer, which can also modify the magnetic properties of the film.

Considering these points, P. Arekapudi suggested, that a sample which does not require annealing or deposition in field should be much easier to prepare in higher quality. Therefore the ferromagnetic layers in the third investigated sample are coupled by a different mechanism. Note that for all of the 3 listed samples, the longitudinal Magneto-Optical Kerr Effect (MOKE) measurements were done by P. Arekapudi.

4.2 BLS measurements

First the thermal spectra of samples with exchange bias (Py/Cu/Py/IrMn) were recorded. Fig. 4.2 illustrates the thermal magnon intensity spectrum for $k = \frac{4\pi}{\lambda_{Laser}} \cos(\theta) = 1.67 \cdot 10^5 \text{ cm}^{-1}$ (incident angle of $\theta = 45^\circ$, $\lambda_{Laser} = 532 \text{ nm}$).

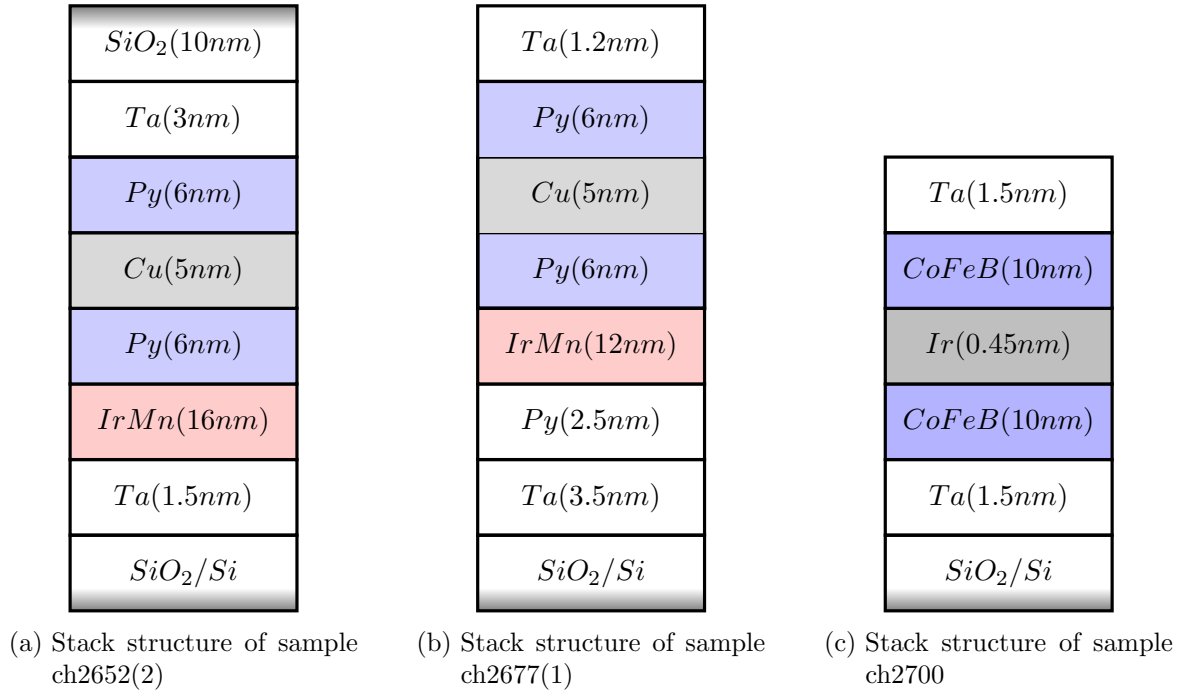


Figure 4.1: Overview of the stack structure of all samples

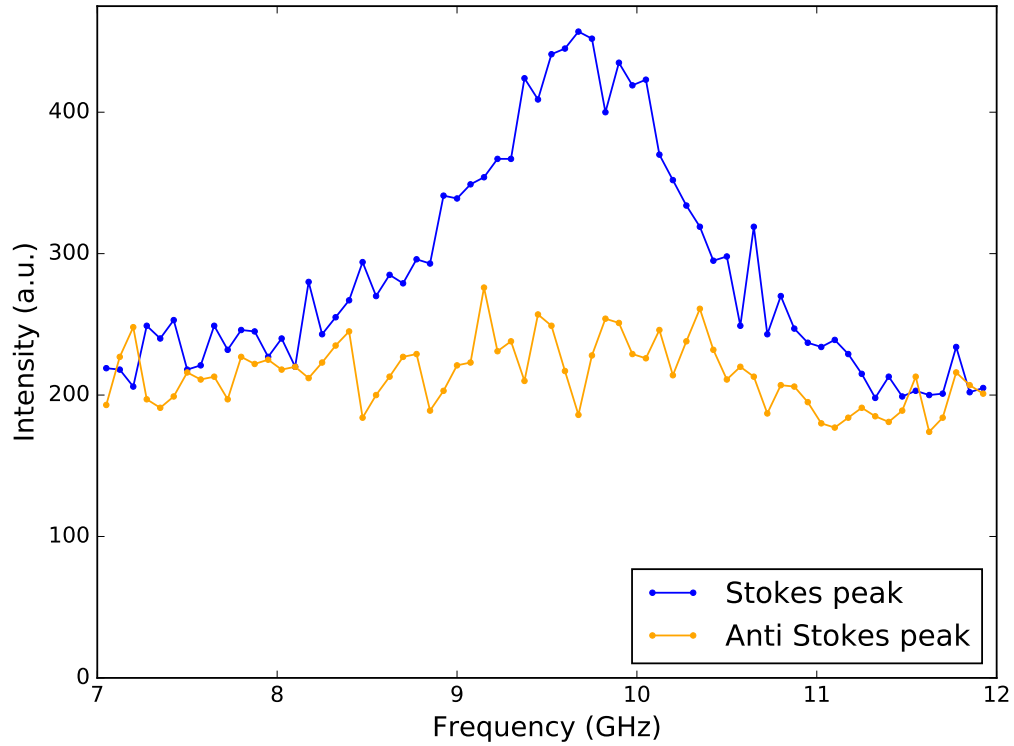


Figure 4.2: Raw BLS spectrum of the sample ch2677(1), incident light at 45 degrees, 39 mW laser power, 60 mT of the external field

It is visible from this raw spectrum that it is quite noisy. The *Stokes* data shows a broad peak and the *anti-Stokes* data seems to not have a peak in intensity at all. After the removal of the background noise and fitting of the data a better picture can be obtained. Fig. 4.3 now shows, that the *Stokes* peak occurs at 9.68 GHz. The fitting routine provides the same 9.68

GHz for the *anti-Stokes* data, however, this result should be treated with a lot of caution, considering the fact, that the initial input data did not feature any pronounced peaks at all. Nevertheless, the obtained result agrees well with the theory, because at 60 mT of the external field the sample is in the ferromagnetic state (see Fig. 4.4a) and no non-reciprocal effects should be observed.

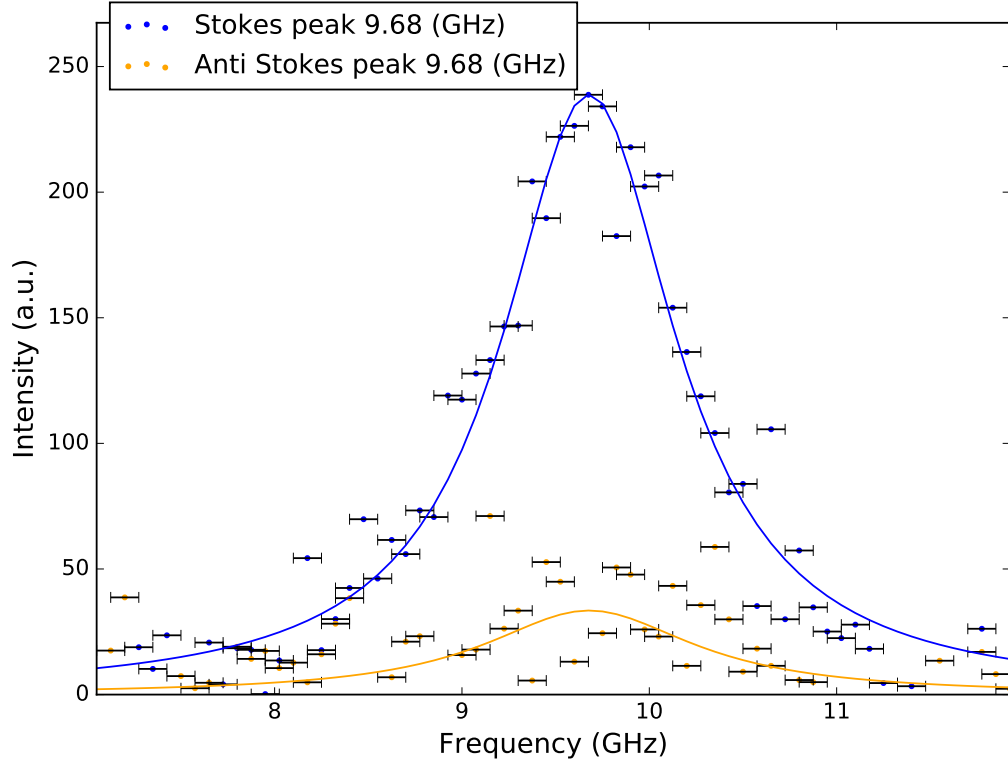
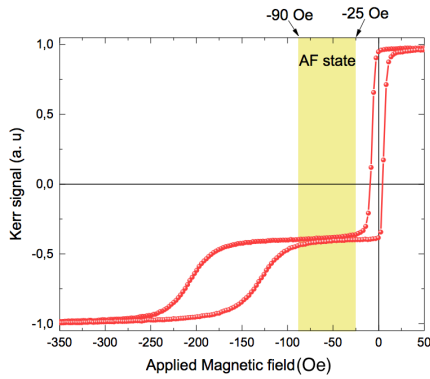
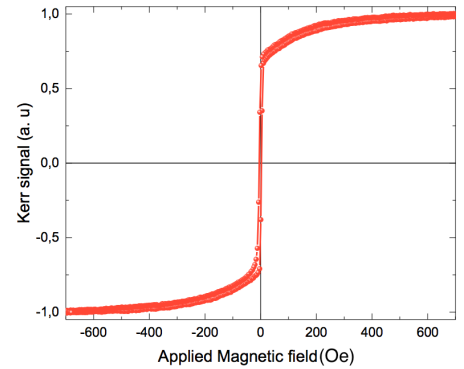


Figure 4.3: Fitted BLS spectrum of the sample ch2677(1), incident light at 45 degrees, 39 mW laser power, 60 mT of external field



(a) Hysteresis loop along the easy axis of the sample ch2700



(b) Hysteresis loop along the hard axis of the sample ch2700

Figure 4.4: Hysteresis curves of the sample ch2677(1), MOKE-measurement done by P.Arekapudi

Measurements at lower external field values proved to be more difficult. For example, a measurement at 6 mT has already such a low signal, that after background noise removal only a *Stokes* peak can be fitted (Fig 4.5a). At 6 mT the sample is in ferromagnetic state, however, there is no way to deduce if the frequencies of the *Stokes* and *anti-Stokes* peaks

differ in any way. The same can be said about the spectrum of Fig. 4.5b, where the sample is in antiferromagnetic state at -6 mT of the external field. Here, only the *anti-Stokes* peak can be observed clearly and fitted. Overall, the sample ch2677(1) was giving low and noisy BLS signals with each measurement requiring a lot of time. It was impossible to compare the frequency difference for $k = 1.67 \cdot 10^5 \text{ cm}^{-1}$ to the predicted theoretical value of $\Delta f = 2.4 \text{ GHz}$, because it is hard to make physical conclusions about the non-reciprocal effects given such spectral content as presented in the Figures 4.3 and 4.5. A possible explanation could be the interdiffusion of the Cu into the Py layers during the annealing procedure. Unfortunately, this could not be investigated in the experiment. Therefore, it is unknown, if the interdiffusion is the main factor of the negative result. For this reasoning, additional conventional BLS measurements on this sample were not considered.

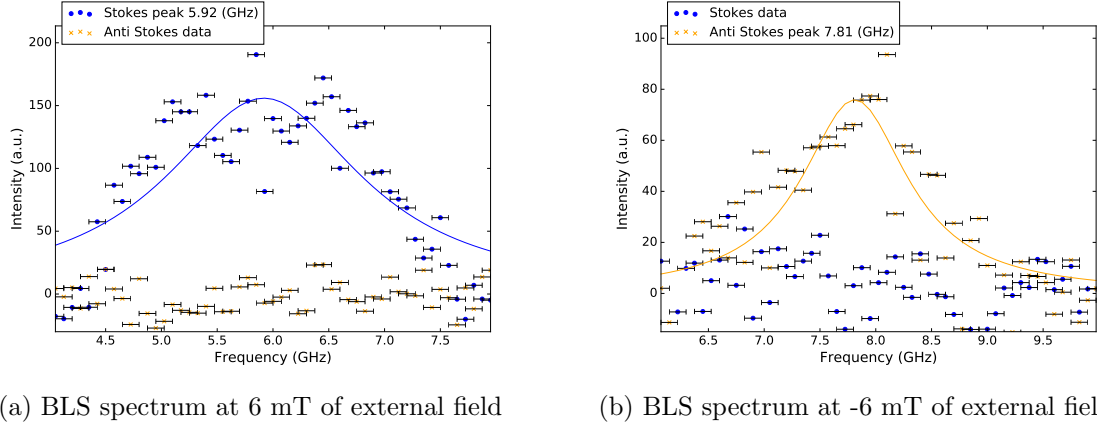


Figure 4.5: BLS spectra of the sample ch2677(1) for $\pm 6 \text{ mT}$ of the external field, incident light at 45 degrees, 39 mW laser power

Next, the sample ch2700 was investigated. The core layer structure of this sample is CoFeB/Ir/CoFeB and the hysteresis loops are given by Fig. 4.6a-4.6b. Taking a closer look at the easy axis loop reveals the antiparallel state of the coupled CoFeB layers from -11 to +5 mT.

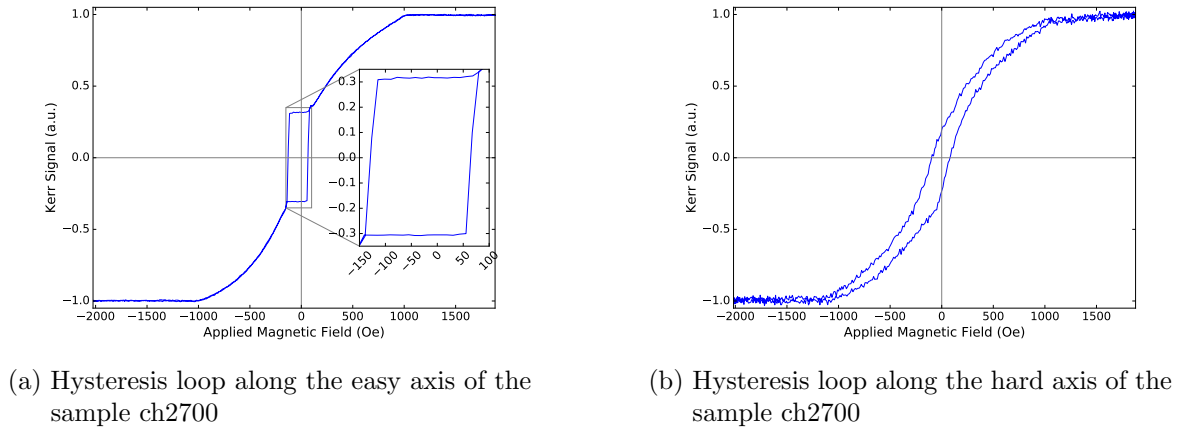


Figure 4.6: Hysteresis curves of the sample ch2700, MOKE-measurement done by P.Arekapudi

As for the previous sample, this sample was investigated at different magnetic fields. Fig. 4.7 shows the SW intensities of the sample for an applied magnetic field of 60 mT along the easy axis of the sample. One thing to point out is that the *anti-Stokes* peak is quite low and noisy which makes it hard to determine precise peak position. Nevertheless, the

frequency difference obtained from this data is $0.22 \text{ GHz} = 220 \text{ MHz}$. From the hysteresis curve Fig.4.6a it is clear, that 60 mT is not enough to fully saturate the film, which could explain the obtained frequency difference.

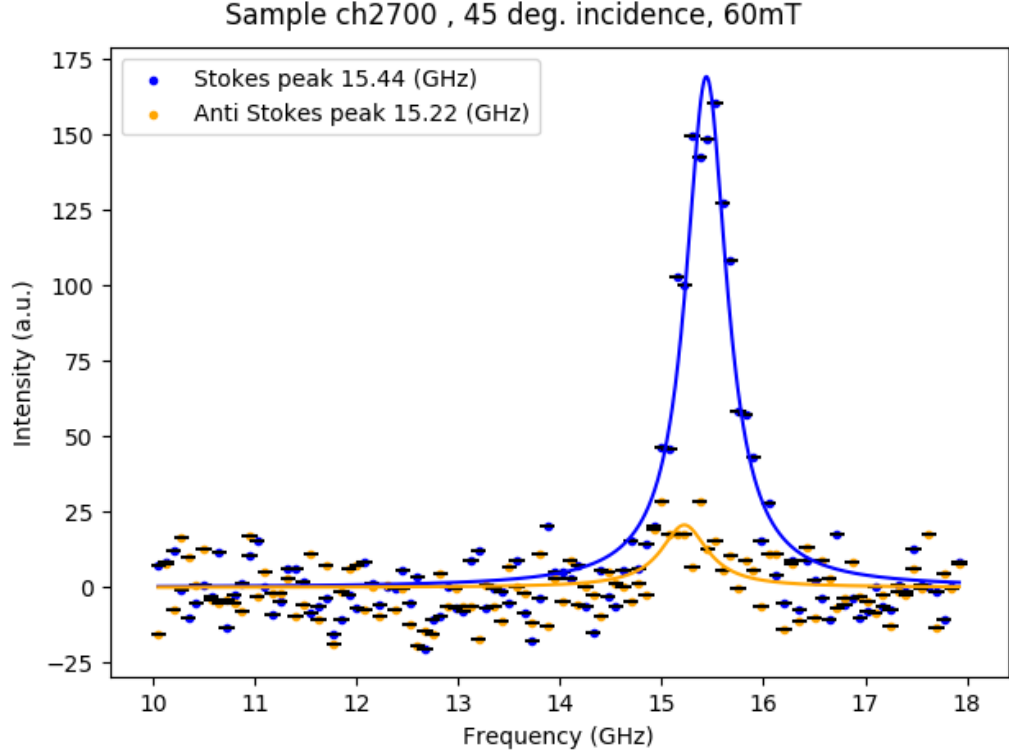


Figure 4.7: BLS spectra of the sample ch2700 at 60 mT of the external field along the easy axis of the sample

According to theoretical predictions non-reciprocal effects should occur in the antiparallel state of the sample. The easy axis hysteresis loop shows, that the sample is in AF state from -11 to $+5 \text{ mT}$. As the sample still is in AF state at zero field, it was decided to collect the BLS spectra without external field. At the start of the measurement sample was always saturated with $+200 \text{ mT}$, then the magnetic field was slowly removed.

For both scenarios either positive or negative saturation the BLS spectra were accumulated. These results are presented by Fig. 4.8 and Fig. 4.9.

Extraction of peak positions of the *Stokes* and *anti-Stokes* signals shows a difference between them for both plots. So for the antiparallel state at 45° incidence, the frequency shift between *Stokes* and *anti-Stokes* signals is on the order of $0.3 \text{ GHz} = 300 \text{ MHz}$. This result should be treated with a lot of caution though, as the obtained peaks are still quite noisy. These graphs at zero field are $\approx 36 \%$ more antisymmetric compared to the spectrum for 60 mT of the external field. But, nevertheless, the obtained frequency difference of 300 MHz is 21 times lower, than the predicted theoretical value of 6.5 GHz for $k = 1.67 \cdot 10^5 \text{ cm}^{-1}$.

Next, the sample was rotated by 90° , so that the magnetic field could be applied along the hard axis of the sample. Here, the same type of experiment at 0 mT was done: sample was saturated with $+200 \text{ mT}$ and then the magnetic field was removed slowly. Fig.4.10 presents the collected BLS spectrum. Interestingly enough, here the frequency difference between the *Stokes* and *anti-Stokes* peaks is $\Delta f = 0.68 \text{ GHz} = 680 \text{ MHz}$ and is twice as high as the frequency difference in the measurements with field along the easy axis of the sample. As the hard axis loop (Fig.4.6b) does not show a double hysteresis behavior, it is unclear, why in this experiment such an effect is observed. However, the frequency difference of $\Delta f = 680$

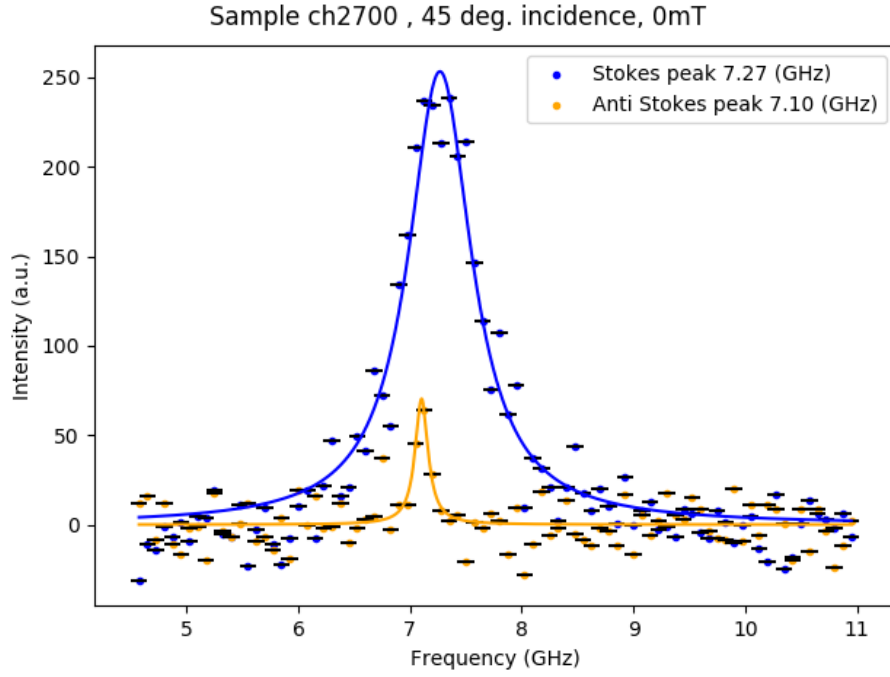


Figure 4.8: BLS spectra of the sample ch2700 at 0 mT, saturated with +200 mT of the external field along the easy axis of the sample

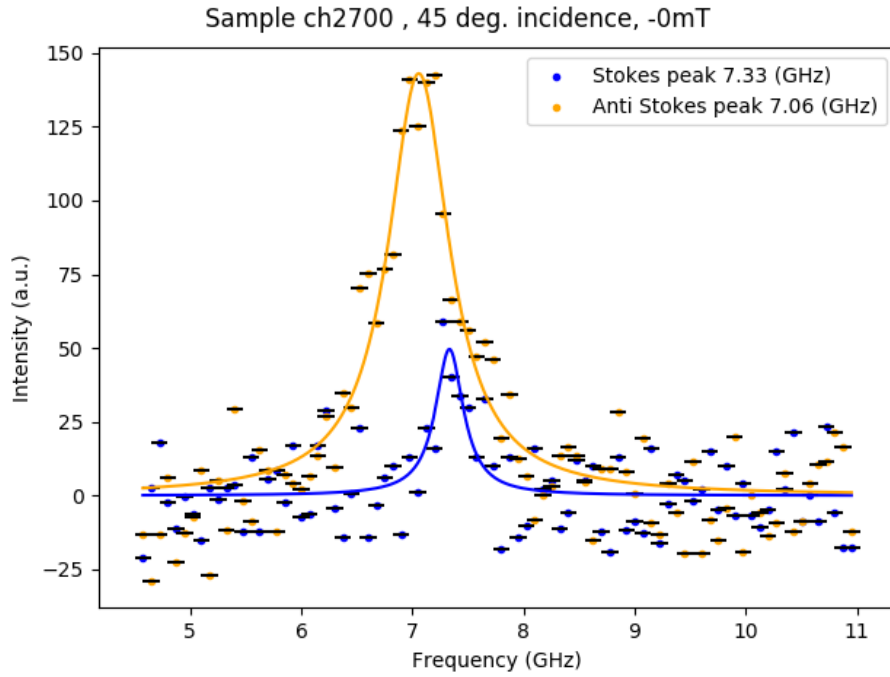


Figure 4.9: BLS spectra of the sample ch2700 at 0 mT, saturated with -200 mT of the external field along the easy axis of the sample

MHz is still 10 times lower than the theoretical value of 6.5 GHz. Therefore, the conclusion about non-reciprocal spin-wave properties of this sample cannot be made with certainty.

Although, the sample ch2700 did not give a clear answer if the the non-reciprocal effects are present and did not match the theoretical expectations, these measurements can be considered as the foundation of study on non-reciprocal effects in such systems. The conven-

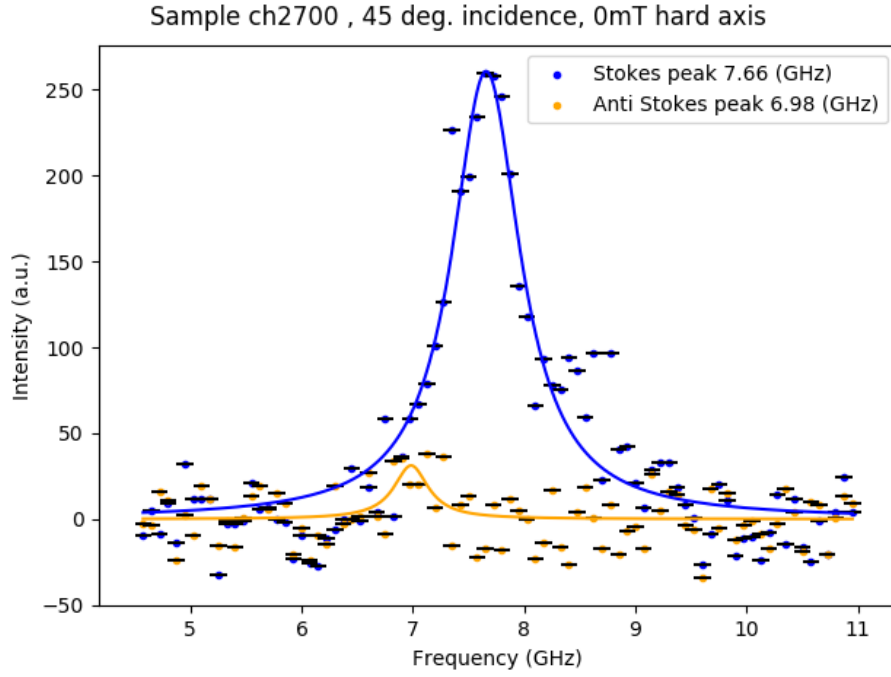


Figure 4.10: BLS spectra of the sample ch2700 at 0 mT, saturated with +200 mT of the external field along the hard axis of the sample

tional BLS gives a good method to probe such films on their quality. Logical continuation is to pattern micro-structures on this films to look at the transport properties. For sample ch2700 this is already planned and will be finished beyond the work of this thesis.

Another sample of a layer structure similar to the one discussed in the beginning of this section was patterned by means of Electron Beam Lithography (EBL), allowing microwave excitation of spin waves and measurements with μ BLS. The results for this sample will be discussed in the next section.

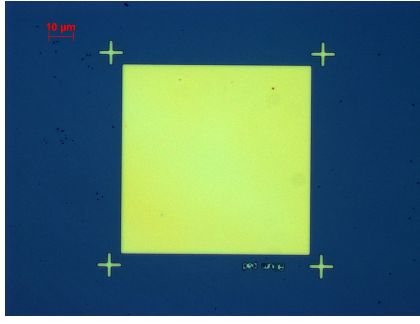
4.3 Micro-BLS measurements

4.3.1 Sample preparation

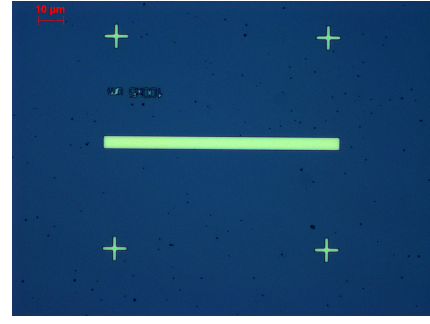
As the μ BLS measurements allow for space- and phase-resolved investigation of spin-wave propagation in magnetic micro-structures one of the samples was patterned by means of electron beam lithography allowing for microwave excitation of spin waves.

At the start, it was planned to pattern the excitation antennas directly on top of the magnetic film in a single lithography step. The antennas design was made such, so that the lithography process consisted of an exposure with two apertures of different sizes for the bigger and smaller parts of the antennas respectively. However, multiple attempts of patterning always had alignment errors. To exclude this alignment problems, the lithography step was changed to include alignment marks. Finally, a 3-step lithography process was carried out to pattern the sample ch2652(2). The details of each step will be discussed next.

In the first step, the sample was spin-coated with 300 nm of negative resist maN-2403. After this, all the magnetic microstructures were written and structured with an argon-based plasma etcher giving two types of geometries - stripes and square pads. Resulting structures are shown by optical micrographs below (Fig. 4.11). Stripes were designed to serve as spin-wave waveguides to later map spin-wave propagation in real space. Square pads were chosen for investigation of caustic beam radiation.



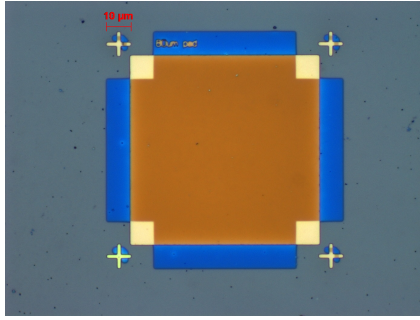
(a) Example of a $80\ \mu\text{m}$ square pad structured on the sample ch2652(2)



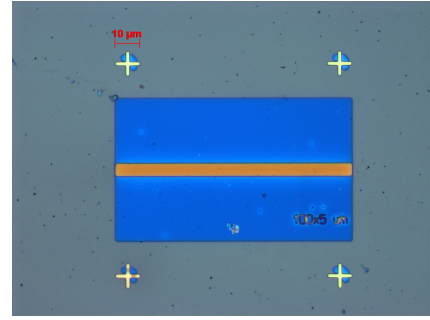
(b) Example of a $100 \times 2\ \mu\text{m}$ stripe structured on the sample ch2652(2)

Figure 4.11: Optical Micrographs after the 1st lithography step

Following this was the coating with 50 nm of Hydrogen silsesquioxane (HSQ) and the second exposure. Exposed HSQ transforms to a perfectly flat SiO_2 layer, allowing for electrical insulation of the magnetic micro-structures from the later deposited excitation antennas. Fig. 4.12 depicts the obtained result.



(a) Example of a $80\ \mu\text{m}$ square pad structured on the sample ch2652(2)



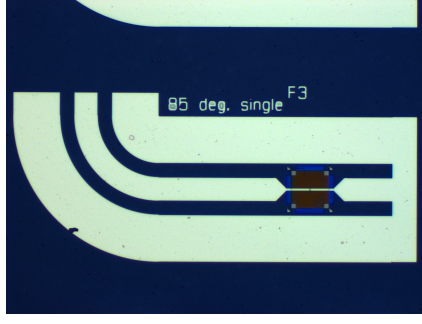
(b) Example of a $100 \times 2\ \mu\text{m}$ stripe structured on the sample ch2652(2)

Figure 4.12: Optical Micrographs after the 2nd lithography step

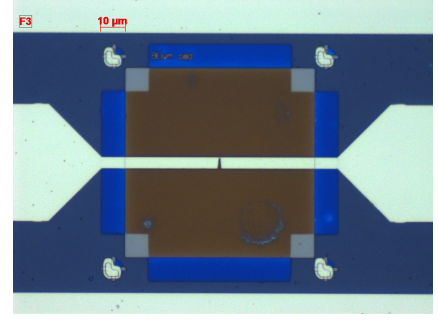
Next, the sample was spin-coated with $\approx 450\ \text{nm}$ of positive resist (PMMA) and the third exposure took place giving a mask for gold deposition for the excitation antennas as the result. The deposition of 160 nm of gold was done in TU Chemnitz by Phani Arekapudi. Finally, the lift-off was done to remove the remaining mask. Fig. 4.13 presents the micrographs of the resulting square pad structure with the antenna for caustics excitation and Fig. 4.14 illustrates the final stripe with the coplanar waveguide for plane wave excitation after liftoff. The coplanar waveguides both for caustics and the plane wave excitation have a spacing of $100\ \mu\text{m}$ between the ground and signal lines so a $100\ \mu\text{m}$ pitch pico-probe can be used to contact these antennas to a microwave generator. All of this work was done with support and materials from the Nanofabrication Center in HZDR.

4.3.2 Eigenmode spectra

To understand the properties of the obtained micro-structured sample, it is advisable to start with measurements of its characteristic spin-wave eigenmodes. There are two principle approaches to do this. First is to measure the μBLS spectra in dependence on the excitation frequency with a fixed external magnetic field. Second is the opposite - measure the BLS spectra in dependence on the applied external field while holding the excitation frequency constant. In this work, both methods were used to characterize the sample.

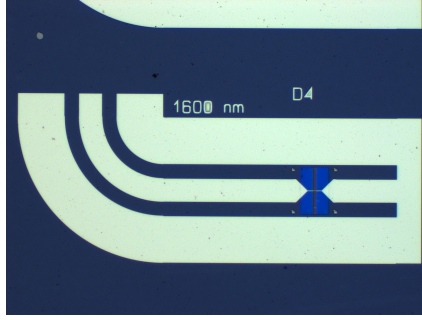


(a) Example of a $80\ \mu\text{m}$ square pad with the excitation antenna

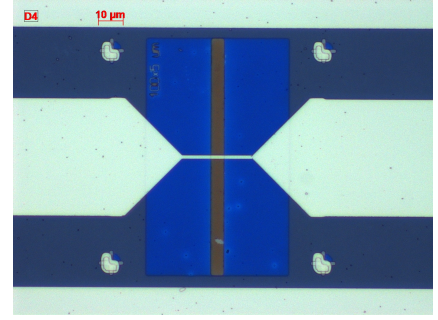


(b) Zoom of a $80\ \mu\text{m}$ square pad with the excitation antenna

Figure 4.13: Optical Micrographs of a pad structure with the excitation antenna after the 3d lithography step



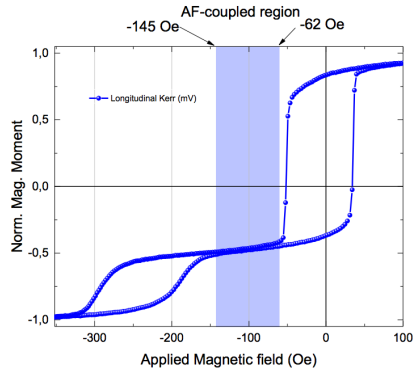
(a) Example of a $100 \times 5\ \mu\text{m}$ stripe with the excitation antenna



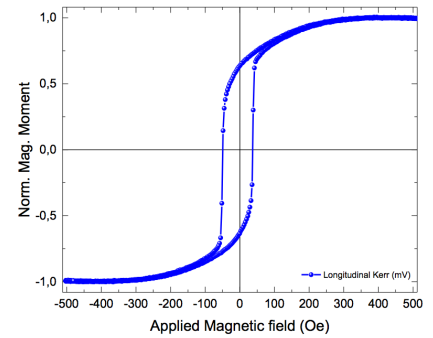
(b) Zoom of a $100 \times 5\ \mu\text{m}$ stripe with the excitation antenna

Figure 4.14: Optical Micrographs of a stripe structure with the excitation antenna after the 3d lithography step

Corresponding to the constant external field method a number of frequency sweeps were done. Fig. 4.15 gives the longitudinal MOKE hysteresis loops along the exchange bias direction and perpendicular to it. First curve shows for which field range the sample is antiparallel where the non-reciprocal effects are predicted to occur.



(a) Hysteresis loop along the exchange bias axis of the sample ch2652(2)



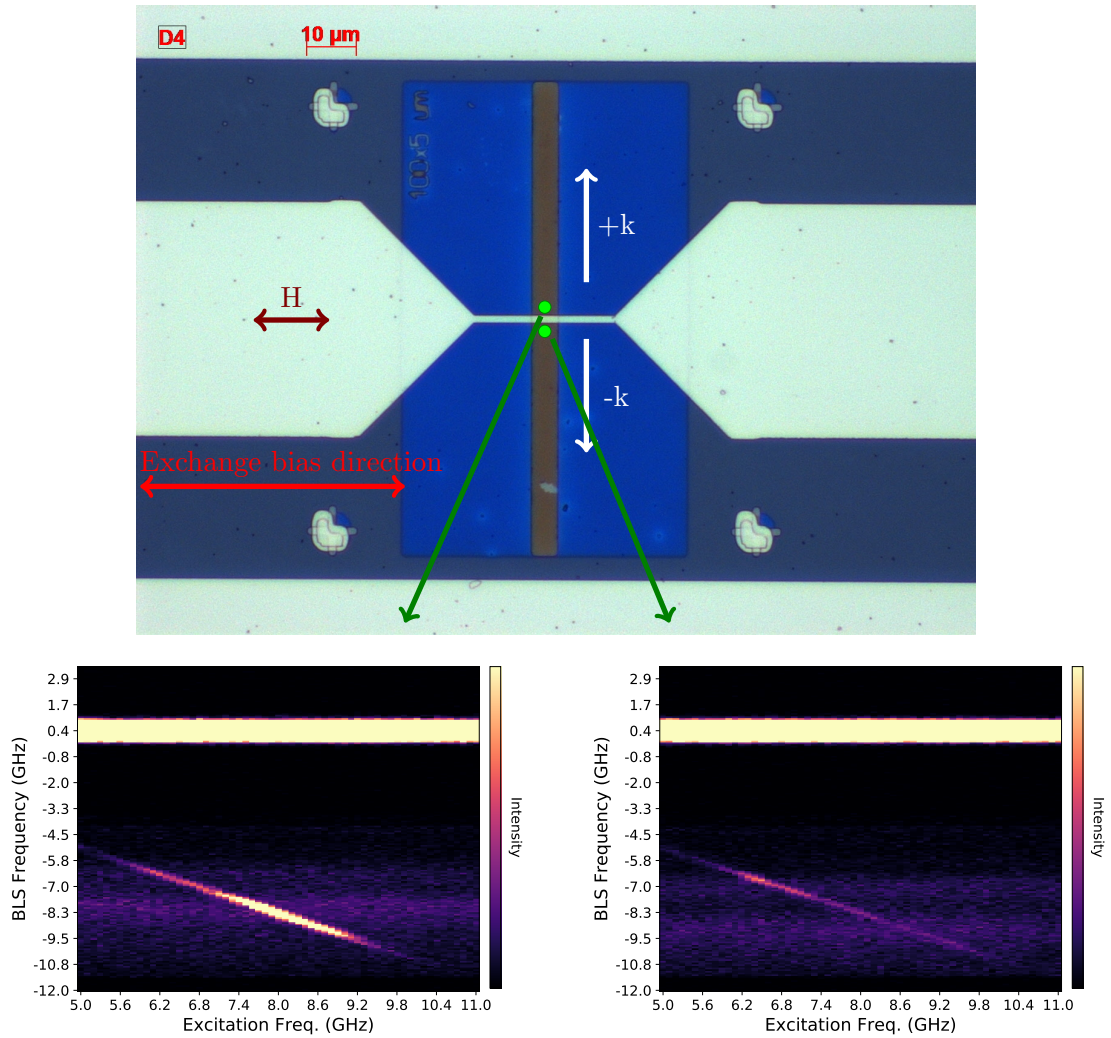
(b) Hysteresis loop along axis perpendicular to the exchange bias axis of the sample ch2652(2)

Figure 4.15: Hysteresis curves of the sample ch2652(2), MOKE-measurements by P. Arekapudi

As a starting measurement, a stripe microstructure was chosen and a frequency sweep was run at a position close to the excitation antenna at 80 mT of the external field applied along the exchange bias direction.

A typical recorded micro-BLS spectra can be presented as a dependence of measured frequency vs the applied microwave frequency with the intensity of spin waves represented by color (Fig. 4.16). As this work is dedicated to the investigation of non-reciprocal effects it is worthwhile to consider measurements for both propagation directions, e.g. above and below the excitation antenna. The measurement positions, as well as field direction with respect to the sample, are given in Fig. 4.16a. If the ferromagnetic layers are aligned parallel the measured spectra of the spin waves should have the same frequencies and only differ in intensity. The difference in intensity could be explained by the fact, that spin waves in the Damon-Eshbach geometry propagate on different surface sides of the thin film for the two opposite directions. The bottom surface of the film is, therefore, giving lower intensity signal for it's respective propagation direction.

(a) Sample micrograph with measurement positions marked by green dots



(b) Measurement position above antenna (+k) (c) Measurement position below antenna (-k)

Figure 4.16: Measured Frequency vs. applied microwave frequency spectra at 80mT

Then the intensity vs applied frequency can be extracted from these spectra. This is done via integration along the diagonals of high intensity visible in the raw data. The resulting

curves can be put on one graph for better comparison and are displayed on Fig. 4.17a. The case of -80 mT is illustrated with Fig. 4.17b. The sample was always saturated with an external field of ± 200 mT respectively before the actual measurement was done. This makes sure the sample was in parallel state during the BLS spectra acquisition.

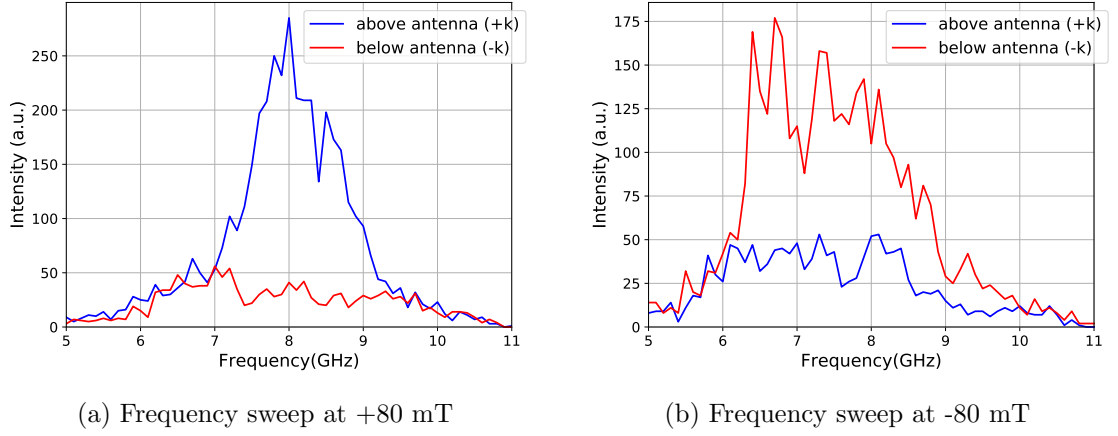


Figure 4.17: Extracted BLS spectra of the frequency sweep at ± 80 mT

It is important to note, that the chosen microwave antenna is exciting a number of wavevectors. Therefore, the frequency sweep spectrum is expected to be rather broad as a whole spin-wave band is excited. From the data shown in Fig. 4.17a it can be seen that for 80 mT of the external field there is a peak-like feature at 8.1 GHz for the position above the excitation antenna. The signal below the antenna, however, does not match this feature. It is unknown, why the frequency content for spin waves of the opposite k -directions varies, as at 80 mT the sample is in ferromagnetic state and the spin-wave dispersion should be reciprocal. In contrary to that, the -80 mT experiment shows similar frequency content for both k -directions. Next, the same experiments were repeated at lower fields of ± 50 mT for same measurement positions (Fig. 4.18).

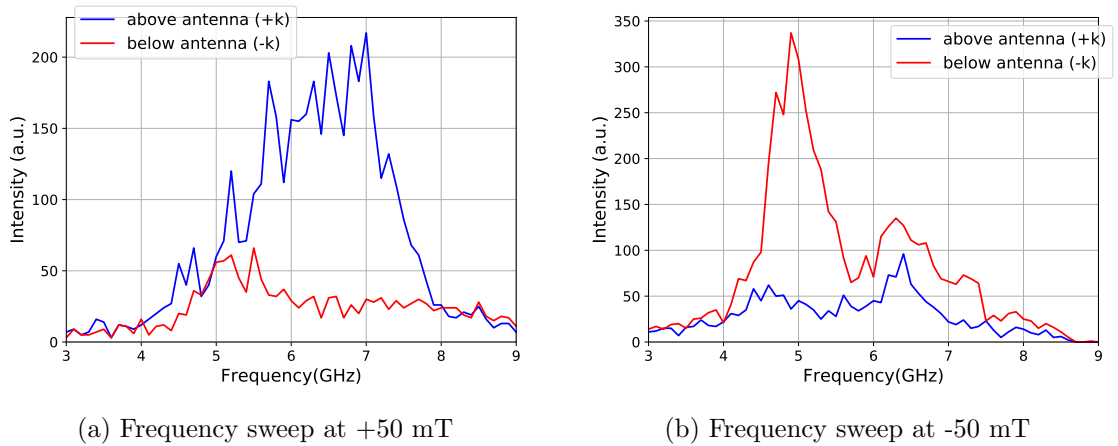


Figure 4.18: Extracted BLS spectra of the frequency sweep at ± 50 mT

For 50 mT case the spectrum curves for $+k$ and $-k$ direction look similar, although the curve for the $-k$ seems to be shifted to lower frequencies. Opposite to this for the -50 mT two peaks are observed, one around 4.9 GHz, another around 6.5 GHz for the $-k$ direction. The $+k$ direction does not have these peaks as much pronounced but the curves look to be identical in the spectral content. Although the measurements at ± 50 mT show the opposite k -directions to be similar for the ferromagnetic state, the quality of these extracted curves

does not allow for a specific statement about any non-reciprocal effects. For this, a mapping of spin-wave intensity in real space along the stripe is needed. However, during a number of different experiments spin-wave signal was disappearing after $1\ \mu\text{m}$ regardless of applied microwave power. This could be explained with the high damping induced by the IrMn antiferromagnet.

Similar to the experiments presented above a measurement at 10 mT of the external field, at which the sample is in antiparallel state, was done. The frequency was swept from 2.5 to 6.0 GHz resulting in spectra for both positions shown in Fig. 4.19.

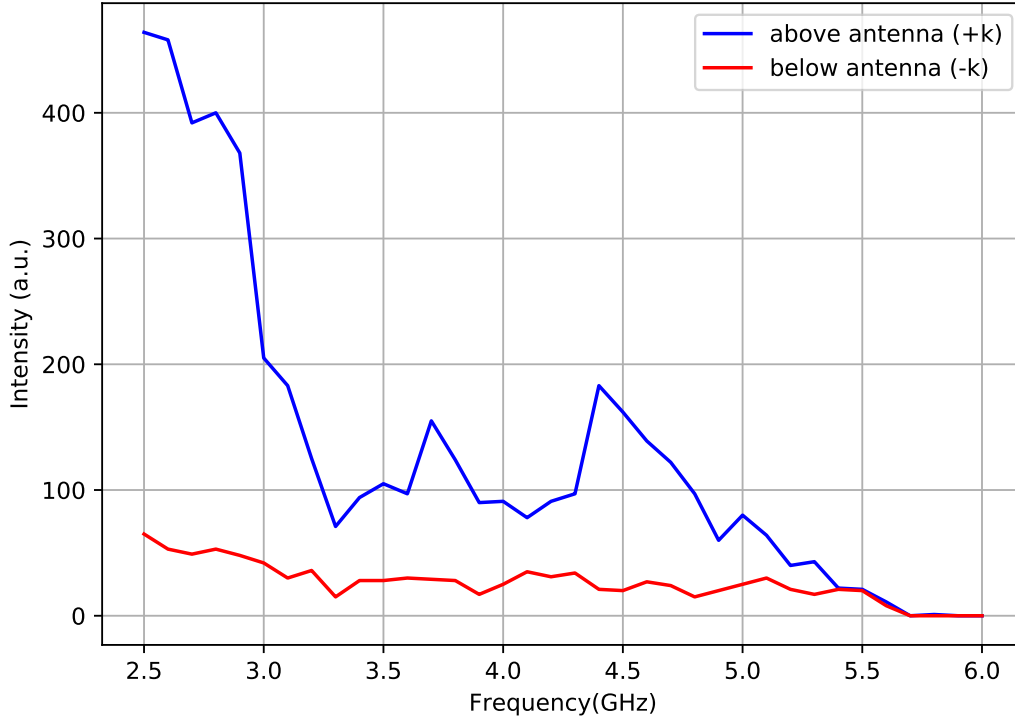


Figure 4.19: Extracted BLS spectrum of the frequency sweep at 10mT of external field

The $+k$ curve starts with high intensity at 2.5 GHz where the measurement started and then falls off with a peak-like feature at 4.4 GHz. The $-k$ data generally has a low signal to noise ratio, but also shows a similar trend at the start of the frequency range. Unfortunately, this spectral content is not enough for a conclusion about non-reciprocal spin-wave propagation.

In a stripe geometry, one always has to be careful about the shape anisotropy which would prefer the alignment of magnetization along the longer dimension of the stripe. The 10 mT of the external field applied to magnetize the sample along its short axis could be not enough to overcome shape anisotropy. Then the sample is in an unclear magnetic state with some domains in it. Because of these uncertainties with the reliability of captured data, it was decided to continue with a square pad structure, where measurements at lower external fields are less affected by shape anisotropy.

The general design of the excitation antennas for the pad structures was done with the idea of caustics measurements in mind. These antennas have a specific shape in the middle which resembles a point-source. However, it is still possible to do measurements to the ones above if one would look at the excitation coming from the flat parts of the antenna.

Similar to the idea for the stripe structure frequency sweeps at ± 80 mT of the external field were done at the positions marked with green on the Fig. 4.20. The raw data for the

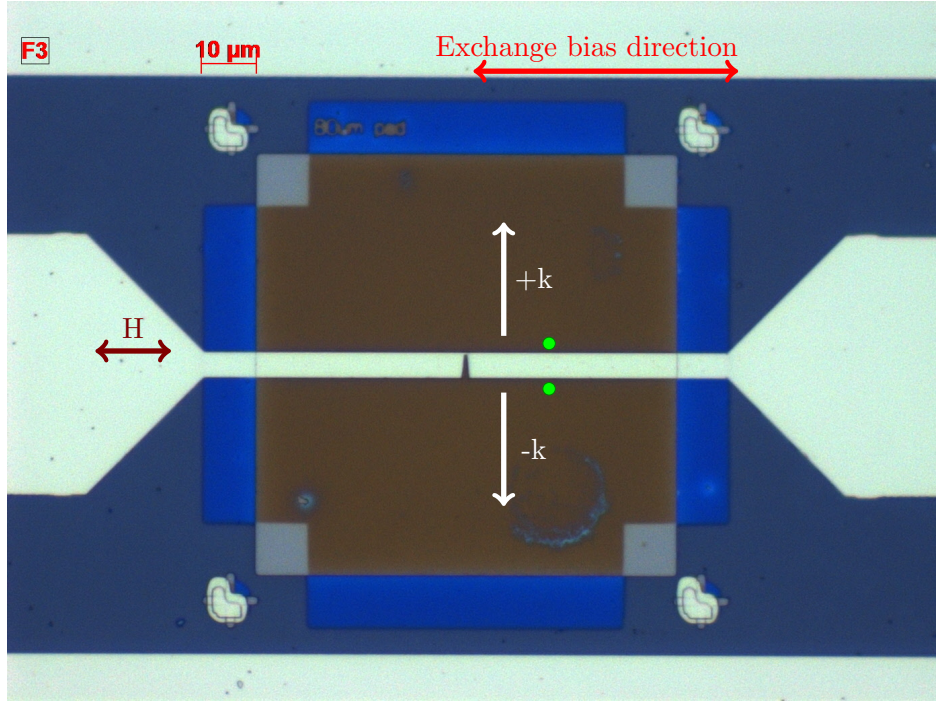


Figure 4.20: Sample micrograph with measurement positions marked by green dots

+80 mT measurement is displayed for both positions is displayed on Fig. 4.21. The frequency was swept from 5 to 11 GHz at 0 dBm of the microwave power.

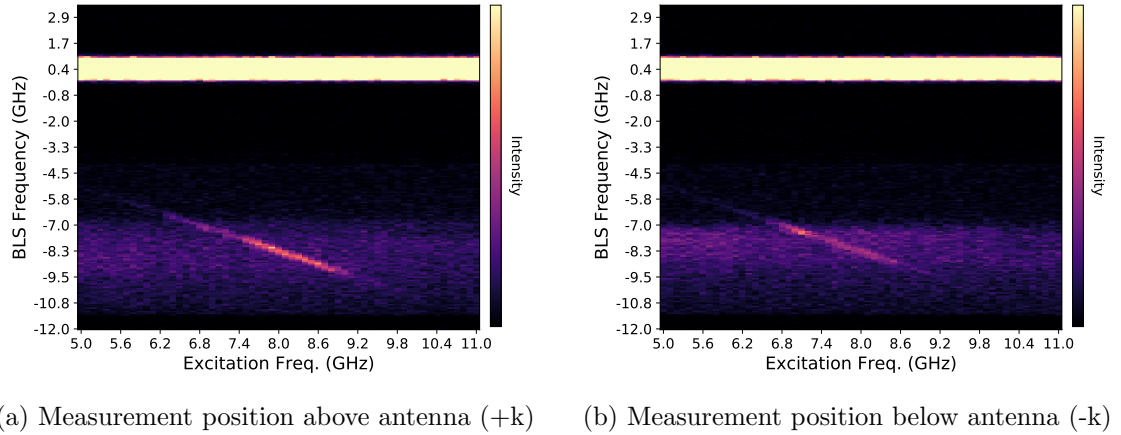
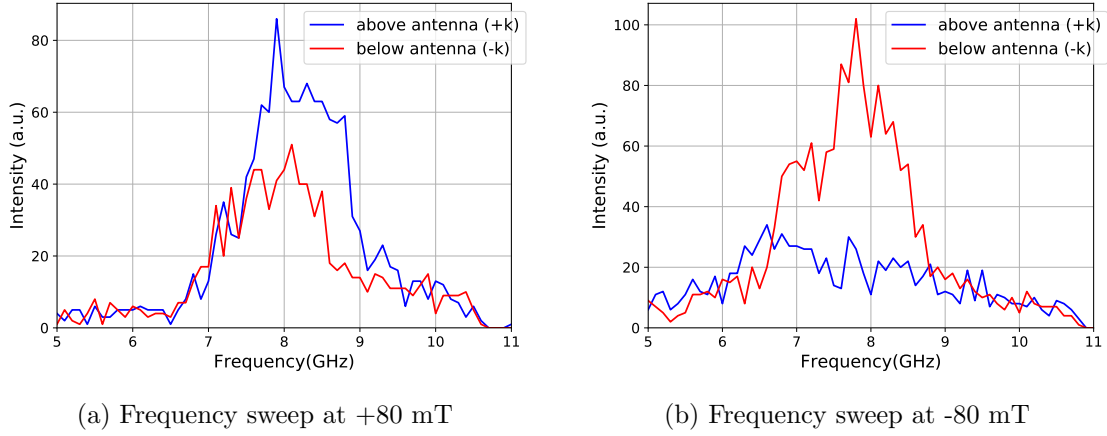


Figure 4.21: Measured Frequency vs. applied microwave frequency spectra at 80mT

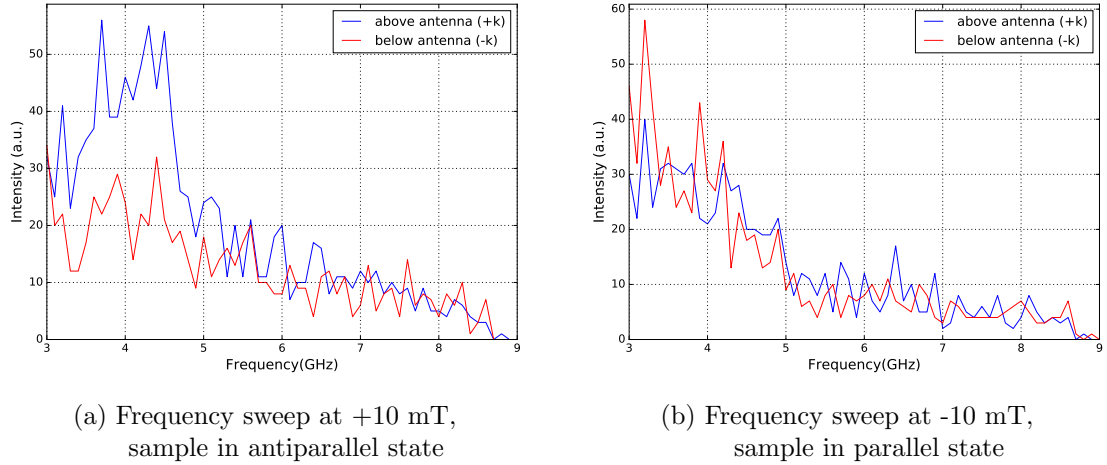
The according extracted intensity vs. frequency curves are depicted by Fig. 4.22.

Taking a look at the Fig. 4.22a for the positive field one can see the similar spectral content of the spectra for both of the k directions. As stated before at 80 mT of the external field the sample is in the parallel state according to the hysteresis loop. Therefore the $+k$ and $-k$ directions should not have anything different other than intensity for a set field. Taking into consideration the very high damping of the sample the 80 mT case fits the expectation to a good extent. However one cannot conclude this for the -80 mT frequency sweep nevertheless the peak frequencies match between both field cases.

Because the focus of this work is in understanding of the non-reciprocal properties of the spin-wave propagation, next measurements were performed at the antiparallel state of the sample, particularly at 10 mT of the external field. Additionally, the same measurement at

Figure 4.22: Extracted BLS spectra of the frequency sweep at ± 80 mT

-10 mT (parallel state) was done as a control experiment. The frequency was swept from 3 to 9 GHz at 0 dBm of microwave power. Resulting spectra are displayed side by side for both measurements on the Fig. 4.23.

Figure 4.23: Extracted BLS spectra of the frequency sweep at ± 10 mT

As expected to be for the parallel case the frequency content of the spectra is very close, despite quite a poor signal to noise ratio. Although the curves for the antiparallel case are different mostly in intensity around 4.0 GHz for the two different measurement positions this data is not enough to make a statement about the unique properties of this sample. The broad peak-like feature around 4.0 GHz attracts further investigation. For a detailed look in the next measurement, the 4.0 GHz excitation frequency was held constant while the external field was now swept from the parallel state through the switching to the antiparallel state and back according to the hysteresis (from 32 mT to -10 mT). The measured intensity vs applied field curve is shown by Fig. 4.24a.

The obtained data, however, gives no insight to the expected in the antiferromagnetic region effects. The attempts to measure at different frequencies were made, but all the gathered spectra looked similar to each other as illustrated by Fig. 4.24. Field sweeps at constant excitation frequency did not prove as an effective method of investigation for this sample. One possible explanation could be that the patterned to micrometer size magnetic material changed its properties so the hysteresis curves (Fig. 4.15) are not anymore a valid reference. As there was no possibility to check the switching behavior of the multilayers directly during

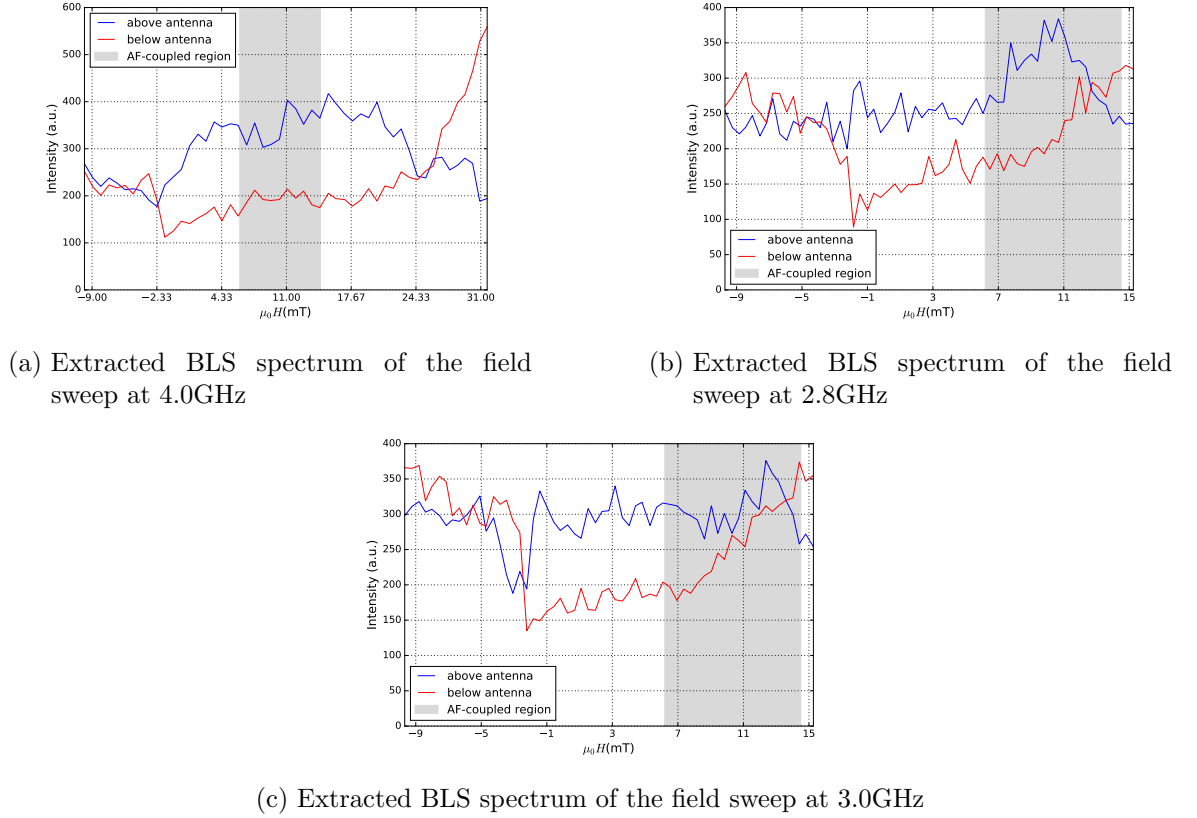


Figure 4.24: Extracted BLS spectra of the field sweeps at different frequencies

the measurement this question can not be answered clearly. Following this logic, the design of structures planned to be patterned in the future was accordingly modified, so there is a possibility of measurements if the layers are in the desired state via the giant-magneto-resistance (GMR) effect. Additionally as already stated before the RKKY-interaction coupled samples have the antiferromagnetic state symmetrically around zero, which also allows for an easy method of measurements without any external field at all.

4.3.3 Caustics measurements

The general idea of the caustics measurements relies on the theoretical prediction, that for these bilayers the caustic angle is expected to change depending on which state the bilayers are currently in. Moreover, in antiparallel state the caustic angle is expected to depend on the excitation frequency.

During the work on this thesis, a number of experiments investigating the caustics radiation was done. First, line scans along the antenna were conducted at a fixed excitation frequency and field of 10 mT as marked by red dots on Fig 4.25.

Fig. 4.26 shows the measured raw spectra for the excitation frequency of 3, 4 and 5 GHz respectively. The peaks of high intensity could have been traced back to the known position in real space allowing to calculate the angle of the caustics radiation. It is visible from the plots, however, that the signal already has significantly less intensity 1 μm from the excitation antenna.

To analyze in more detail, the intensity can be summed up along the excitation frequency for both of the presented measurement position line scans. Below in Fig. 4.27 are the integrated intensity over the position along the antenna.

From this data it is visible, that mainly direct excitation from the antenna occurring, as

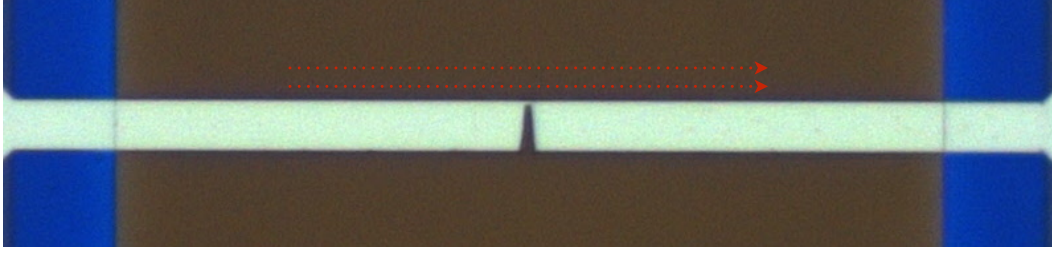
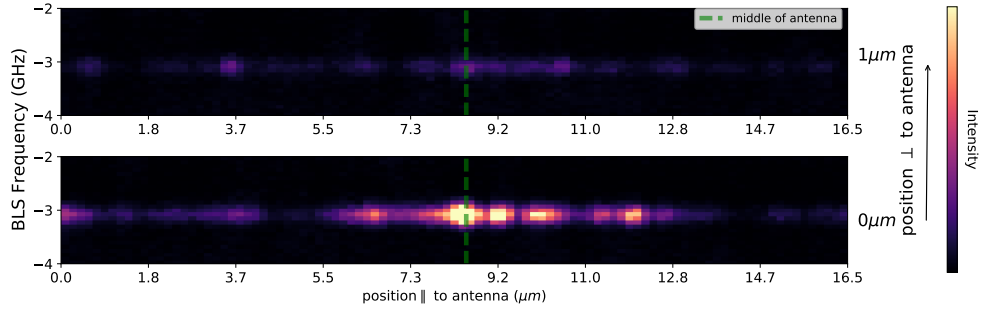
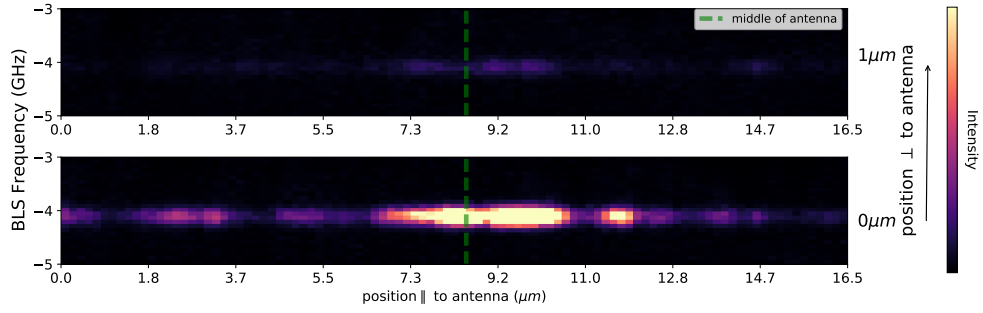


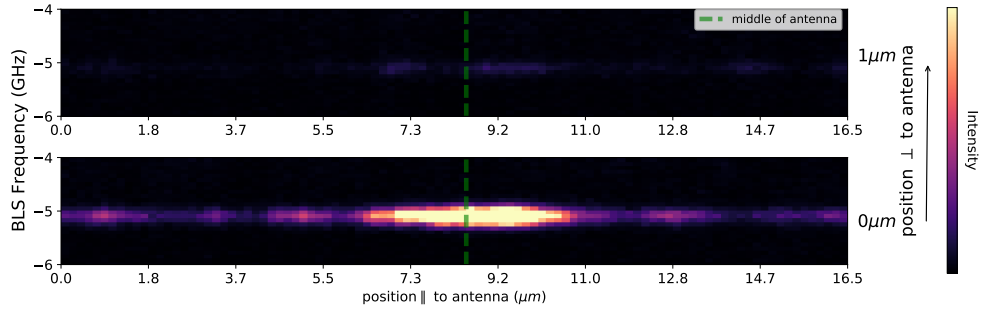
Figure 4.25: Sample micrograph with measurement positions marked by red dots, arrows indicate the direction of the line scans



(a) Measured spectra for 3 GHz



(b) Measured spectra for 4 GHz



(c) Measured spectra for 5 GHz

Figure 4.26: Raw Spectra for line scans along the antenna for different excitation frequencies at 10 mT

the main intensity is radiated from the center of the antenna where the notch is located. Moreover the intensity 1 μm distance from the antenna already is too low to extract certain peak positions. From this data it is impossible to tell if there are at all caustics being radiated under some angle.

In continuation of the caustics measurements, radial scans were performed next with help

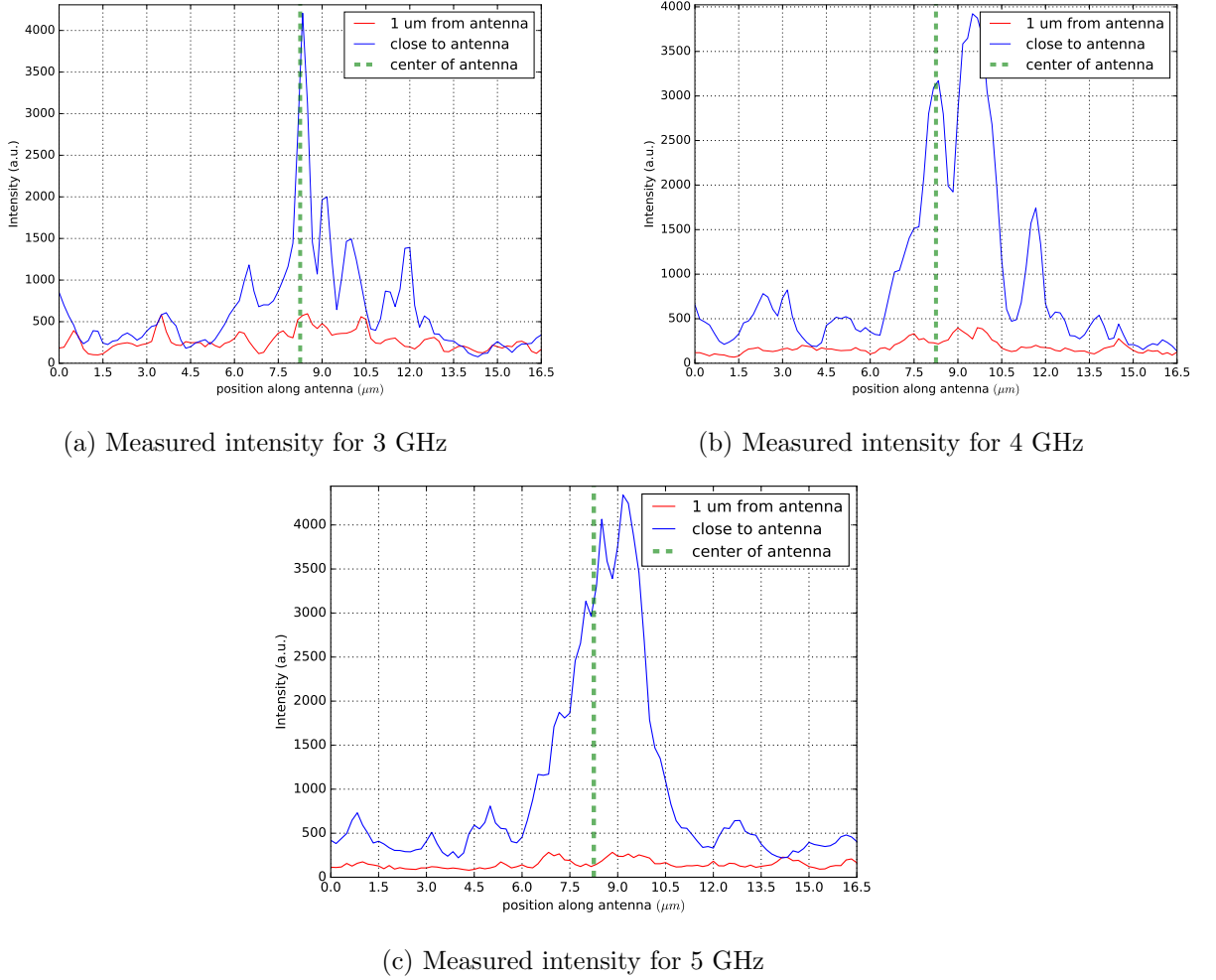


Figure 4.27: Measured intensity for the selected line scans at 3, 4, 5 GHz respectively, ext. field = 10 mT

of Dr. N. Nishida. For a set of excitation frequencies the BLS spectra were recorded for 3 radial scans of 1, 2, 3 μm in radius around the center of the excitation antenna and the external field was held at 10 mT. Fig. 4.28 shows the image made by the micro-BLS camera during the measurement. The crosshair marks the position of the middle of the laser spot, the 3 circles mark the circular scans performed in this measurement.

For each of the circular scans of different radius, the intensity can be mapped on a radial plot (Fig. 4.29). Taking a closer look at the angular intensity distribution at 1 μm distance from antenna one can make a conclusion, that mainly a direct excitation is occurring. The 2 μm distance also seems to be influenced by the direct excitation from the different parts of the antenna.

As it was pointed out before, in the previous measurements done for this sample the propagation length of the spin waves is quite low as the signal intensity drops dramatically on distances further than 1 μm from the excitation point. For this reasoning, it is hard to exclude that the measured in circular scans intensity is coming specifically from the caustic beams. The measured data is more likely an interference coming from the spin waves excited from the notch representing the point source and spin waves directly excited by wider parts of the antenna. So for further investigation of the angles of the caustic beams the distances of 1 and 2 μm cannot be treated as good reference points. Therefore, further the circular scans of 3 μm in radius will be discussed.

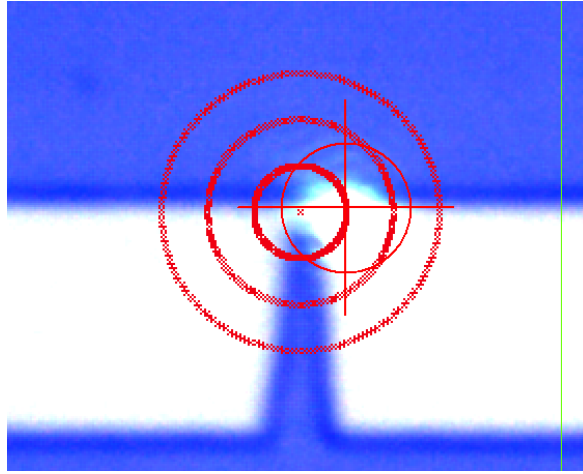
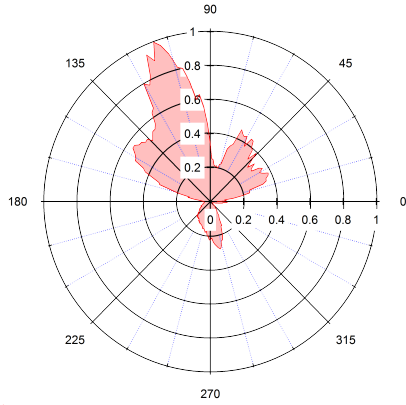
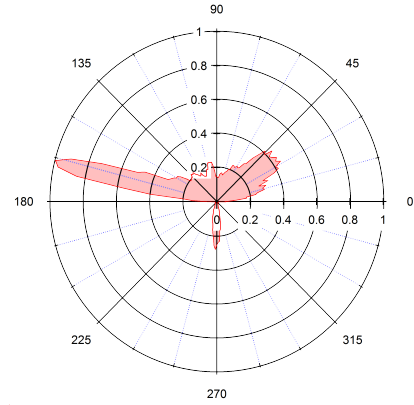


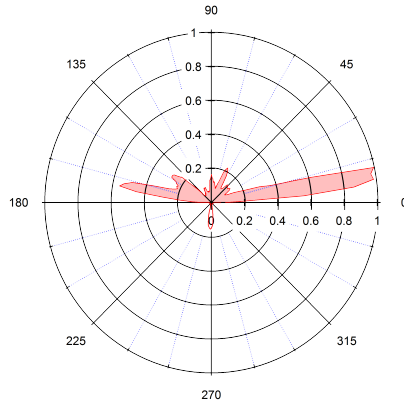
Figure 4.28: MicroBLS camera image of the sample, the circular scans are marked by red points, the red crosshair marks the position of the middle of the laser spot



(a) 1 μm circular scan at 3 GHz excitation



(b) 2 μm circular scan at 3 GHz excitation



(c) 3 μm circular scan at 3 GHz excitation

Figure 4.29: Radial intensity maps for each measured circular scan, figures courtesy of Dr. N. Nishida

As was already shown in section 2.5 of the Theory chapter, the angle of the radiated caustic beams should vary with the applied excitation frequency. Fig. 4.30 compares the

obtained data for excitation for selected excitation frequencies of 3, 3.4, 3.6 and 4 GHz at the $3\text{ }\mu\text{m}$ distance from the notch of the antenna. The presented plots make it clear, that for the obtained data no angular dependence with frequency is observed.

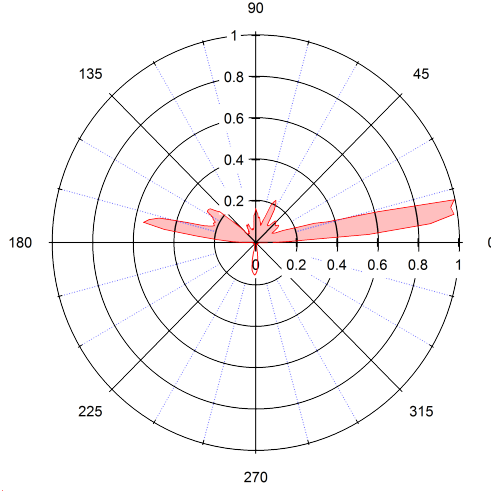
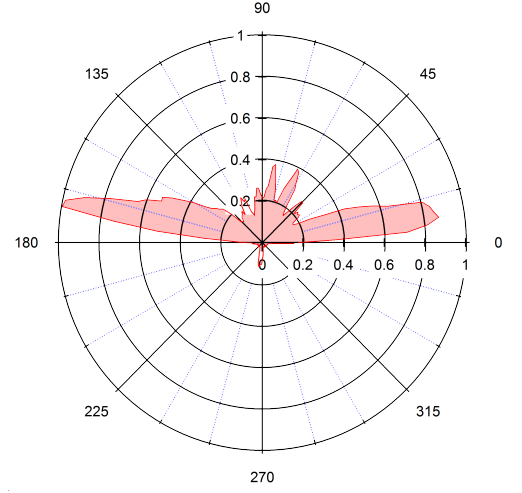
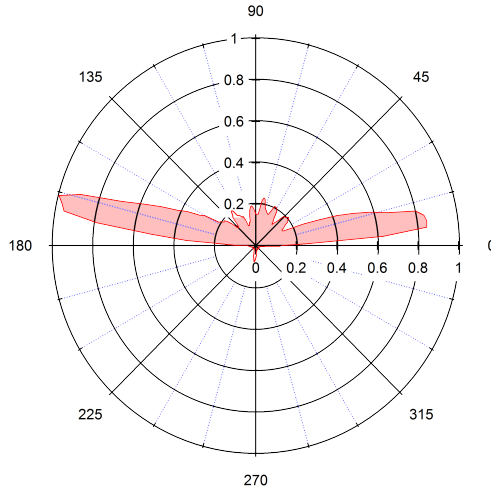
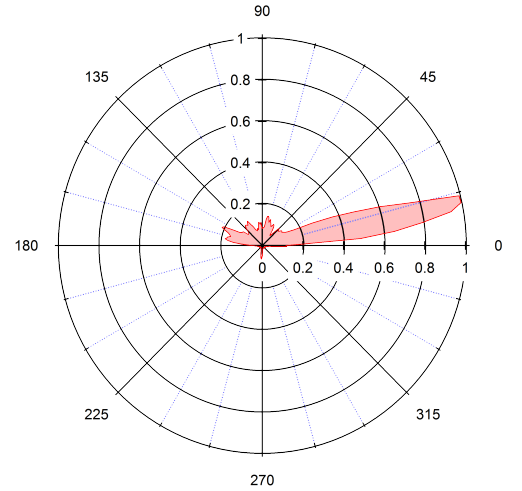
(a) $3.0\text{ }\mu\text{m}$ circular scan at 3 GHz excitation(b) $3\text{ }\mu\text{m}$ circular scan at 3.4 GHz excitation(c) $3\text{ }\mu\text{m}$ circular scan at 3.6 GHz excitation(d) $3\text{ }\mu\text{m}$ circular scan at 4.0 GHz excitation

Figure 4.30: Comparison of the measured intensity at $3\text{ }\mu\text{m}$ distance for different excitation frequencies, figures courtesy of Dr. N. Nishida

This result may be explained as follows. The measured signal is still mainly consistent from the spin waves directly excited from the antenna and not the caustic beams. All measurements done on this sample lead to one conclusion: regardless of the tried out measurement techniques the high damping of the sample makes it impossible to observe the theoretically predicted effects. Additionally, the selected geometry of the excitation antenna could be not optimal for caustic beam excitation. For further investigation in such systems, all of this points must be considered with caution.

5 Summary and Outlook

A central point of this Master thesis was the investigation of non-reciprocal spin-wave dispersion in coupled bilayers. For this purpose, a conventional Brillouin Light Scattering setup was assembled. This made the measurements on thermally excited spin waves possible. The explored bilayer systems had two different approaches towards the realization of the anti-ferromagnetic alignment between the coupled layers, the exchange bias and the interlayer exchange interaction. Both were probed with the assembled conventional BLS setup. Additionally, one of the initial magnetic films with exchange bias was microstructured by means of electron beam lithography. Then the transport properties of spin waves excited by local microwave fields were researched with a BLS-microscope. The possibility of caustic beam radiation was explored as well.

Although I successfully tested the working condition of the conventional BLS setup with reference films, experiments have not proven to be effective for the sample with the exchange bias. The thermally excited spin waves in this film did not give reliable signals with a reasonable signal to noise ratio, therefore, no conclusions on the agreement with the theoretical predictions could be made. The sample with the interlayer exchange interaction did show non-reciprocal spin-wave behavior in the experiments, although the observed effect was a factor of 10 lower than the expected theoretical value. Despite the disagreement with the theory, this sample shows the desired effect and will be tested with respect to the spin-wave transport in the future. It will be patterned and investigated further with the BLS-microscope beyond the work of this thesis and within the framework of the collaboration with R.A. Gallardo, A. Roldán-Molina, and P. Landeros on this project in general.

During the work on this thesis, I successfully patterned the sample by means of electron beam lithography. The μ BLS experiments on the patterned sample gave a lot of insight on the possible improvements and ideas for further sample production and new excitation antenna geometries. The sample with the exchange bias proved to be unsuitable for spin-wave transport, as the IrMn antiferromagnet, which induces the exchange bias, is believed to increase damping of the bilayer system in total. The experiments have shown that, although whole spin-wave bands can be excited, the damping of the system is too high for spin-wave propagation on distances larger than 1 μm .

The experiments of caustic beam radiation for different frequencies can be used as a foundation for further research in this direction. The selected excitation antenna design was ineffective due to damping effects for the particular sample investigated during the experiments in connection with this thesis.

Summing up, this thesis is the first step in the research towards the usage of the non-reciprocal effects in coupled bilayer systems for the realization of spin-wave devices based on spin-wave caustic beams radiation. A lot more work is needed to get a better insight in the experimental properties of the coupled bilayer systems.

Bibliography

- [1] T. Schneider et al. “Realization of spin-wave logic gates”. In: *Applied Physics Letters* 92.2 (2008), p. 022505. DOI: 10.1063/1.2834714. eprint: <http://dx.doi.org/10.1063/1.2834714>. URL: <http://dx.doi.org/10.1063/1.2834714>.
- [2] K.-S. Lee and S.-K. Kim. “Conceptual design of spin wave logic gates based on a Mach–Zehnder-type spin wave interferometer for universal logic functions”. In: *Journal of Applied Physics* 104.5 (2008), p. 053909. DOI: 10.1063/1.2975235. eprint: <http://dx.doi.org/10.1063/1.2975235>. URL: <http://dx.doi.org/10.1063/1.2975235>.
- [3] A. Khitun, M. Bao, and K. L. Wang. “Magnonic logic circuits”. In: *Journal of Physics D: Applied Physics* 43.26 (2010), p. 264005. URL: <http://stacks.iop.org/0022-3727/43/i=26/a=264005>.
- [4] N. Sato, K. Sekiguchi, and Y. Nozaki. “Electrical Demonstration of Spin-Wave Logic Operation”. In: *Applied Physics Express* 6.6 (2013), p. 063001. URL: <http://stacks.iop.org/1882-0786/6/i=6/a=063001>.
- [5] K. Wagner et al. “Magnetic domain walls as reconfigurable spin-wave nanochannels”. In: *Nature nanotechnology* 11.5 (2016), pp. 432–436.
- [6] T. Schneider et al. “Nondiffractive Subwavelength Wave Beams in a Medium with Externally Controlled Anisotropy”. In: *Phys. Rev. Lett.* 104 (19 2010), p. 197203. DOI: 10.1103/PhysRevLett.104.197203. URL: <https://link.aps.org/doi/10.1103/PhysRevLett.104.197203>.
- [7] G. Csaba, A. Papp, and W. Porod. “Spin-wave based realization of optical computing primitives”. In: *Journal of Applied Physics* 115.17 (2014), p. 17C741. DOI: 10.1063/1.4868921. eprint: <http://dx.doi.org/10.1063/1.4868921>. URL: <http://dx.doi.org/10.1063/1.4868921>.
- [8] S. Klingler et al. “Design of a spin-wave majority gate employing mode selection”. In: *Applied Physics Letters* 105.15 (2014), p. 152410. DOI: 10.1063/1.4898042. eprint: <http://dx.doi.org/10.1063/1.4898042>. URL: <http://dx.doi.org/10.1063/1.4898042>.
- [9] K. Vogt et al. “Realization of a spin-wave multiplexer”. In: 5 (Apr. 2014), 3727 EP –. URL: <http://dx.doi.org/10.1038/ncomms4727>.
- [10] K. Di et al. “Direct Observation of the Dzyaloshinskii-Moriya Interaction in a Pt/Co/Ni Film”. In: *Physical Review Letters* 114.4, 047201 (Jan. 2015), p. 047201. DOI: 10.1103/PhysRevLett.114.047201. arXiv: 1409.8570 [cond-mat.mtrl-sci].

- [11] K. Di et al. “Asymmetric spin-wave dispersion due to Dzyaloshinskii-Moriya interaction in an ultrathin Pt/CoFeB film”. In: *Applied Physics Letters* 106.5, 052403 (Feb. 2015), p. 052403. DOI: 10.1063/1.4907173. arXiv: 1412.3907 [cond-mat.mes-hall].
- [12] J.-V. Kim, R. L. Stamps, and R. E. Camley. “Spin wave power flow and caustics in ultrathin ferromagnets with the Dzyaloshinskii-Moriya interaction”. In: *Physical review letters* 117.19 (2016), p. 197204.
- [13] A. Haldar, C. Tian, and A. O. Adeyeye. “Isotropic transmission of magnon spin information without a magnetic field”. In: *Science Advances* 3.7 (2017), e1700638.
- [14] L. Landau and E. Lifshitz. “On the theory of the dispersion of magnetic permeability in ferromagnetic bodies”. In: *Phys. Z. Sowjetunion* 8.153 (1935), pp. 101–114.
- [15] H. Schultheiß. *Brillouin-Lichtstreu-Mikroskopie an magnetischen Mikrostrukturen*. Diplomarbeit. Technical University of Kaiserslautern, 2005.
- [16] T. L. Gilbert. “A phenomenological theory of damping in ferromagnetic materials”. In: *IEEE Transactions on Magnetism* 40.6 (2004), pp. 3443–3449. ISSN: 0018-9464. DOI: 10.1109/TMAG.2004.836740.
- [17] S. Chikazumi. *Physics of Magnetism*. John Wiley & Sons.
- [18] C. C. Tannoudji, B. Diu, and F. Laloe. *Quantum Mechanics*. John Wiley & Sons.
- [19] J. Stöhr and H. C. Siegmann. *Magnetism. From Fundamentals to Nanoscale Dynamics*. Vol. 152. Solid-State Sciences. Springer, 2006.
- [20] C. Kittel. “On the Theory of Ferromagnetic Resonance Absorption”. In: *Phys. Rev.* 73 (2 1948), pp. 155–161. DOI: 10.1103/PhysRev.73.155. URL: <https://link.aps.org/doi/10.1103/PhysRev.73.155>.
- [21] C. Herring and C. Kittel. “On the Theory of Spin Waves in Ferromagnetic Media”. In: *Phys. Rev.* 81 (5 1951), pp. 869–880. DOI: 10.1103/PhysRev.81.869. URL: <https://link.aps.org/doi/10.1103/PhysRev.81.869>.
- [22] B. A. Kalinikos and A. N. Slavin. “Theory of dipole-exchange spin wave spectrum for ferromagnetic films with mixed exchange boundary conditions”. In: *Journal of Physics C: Solid State Physics* 19.35 (1986), p. 7013. URL: <http://stacks.iop.org/0022-3719/19/i=35/a=014>.
- [23] R. Damon and J. Eshbach. “Magnetostatic modes of a ferromagnet slab”. In: *Journal of Physics and Chemistry of Solids* 19.3 (1961), pp. 308–320. ISSN: 0022-3697. DOI: [https://doi.org/10.1016/0022-3697\(61\)90041-5](https://doi.org/10.1016/0022-3697(61)90041-5). URL: <http://www.sciencedirect.com/science/article/pii/0022369761900415>.
- [24] C. L. Ordóñez-Romero et al. “Three-magnon splitting and confluence processes for spin-wave excitations in yttrium iron garnet films: Wave vector selective Brillouin light scattering measurements and analysis”. In: *Phys Rev B* 79.14, 144428 (Apr. 2009), p. 144428. DOI: 10.1103/PhysRevB.79.144428.
- [25] W. Demtröder. *Experimentalphysik 2*. Vol. 10. Elektrizität und Optik. Springer, 1995.
- [26] J. R. Sandercock. “High Contrast Tandem Fabry-Perot Interferometer TFP-2 HC”. In: *Operators Manual* (2005). URL: <http://www.tablestable.com/en/products/view/39/>.
- [27] B. Hillebrands. “Progress in multipass tandem Fabry-Perot interferometry: I. A fully automated, easy to use, self-aligning spectrometer with increased stability and flexibility”. In: *Review of Scientific Instruments* 70.3 (1999), pp. 1589–1598. DOI: 10.1063/1.1149637. eprint: <http://dx.doi.org/10.1063/1.1149637>. URL: <http://dx.doi.org/10.1063/1.1149637>.

- [28] F. Lord Rayleigh. “XXXI. Investigations in optics, with special reference to the spectro-scope”. In: *Philosophical Magazine* 8.49 (1879), pp. 261–274. DOI: 10.1080/14786447908639684. eprint: <http://dx.doi.org/10.1080/14786447908639684>. URL: <http://dx.doi.org/10.1080/14786447908639684>.

Acknowledgements

I would like to thank

Dr. H. Schultheiß for the selection of the interesting research topic, supervision of the project and overall patience and support throughout all stages of my Master thesis.

P. Arekapudi for the preparation of the samples for the project and the MOKE characterization of them.

T. Schneider for all the theoretical calculations.

Dr. N Nishida, Dr. L. Fallarino and K. Wagner for their help with measurements, fruitful discussions and a lot valuable advice.

C. Neisser, T. Schönherr, T. Hache for a lot of useful information regarding the electron beam lithography patterning.

I am very grateful to my grandfather for the hours of proofreading and corrections of my thesis.

A very special gratitude goes to my family and all of my friends, whose continuous support was very motivating.

And finally, I would like to thank all other unnamed scientists of the Institute of Ion Beam Physics and Materials Research for the nice atmosphere.

Statement of authorship

I hereby certify that I have authored this Master Thesis entitled *Non Reciprocal Behavior of Spin Waves in Coupled Layers* independently and without undue assistance from third parties. No other than the resources and references indicated in this thesis have been used. I have marked both literal and accordingly adopted quotations as such. There were no additional persons involved in the intellectual preparation of the present thesis. I am aware that violations of this declaration may lead to subsequent withdrawal of the degree.

Dresden, 30.10.2017

Peter Matthies